3-2015

Langmuir Turbulence under Hurricane Gustav (2008)

Tyler J. Rabe

Tobias Kukulka

Isaac Ginis
University of Rhode Island, iginis@uri.edu

Tetsu Hara
University of Rhode Island, thara@uri.edu

Brandon G. Reichl

See next page for additional authors

Citation/Publisher Attribution

Rabe, Tyler J.; Kukulka, Tobias; Ginis, Isaac; Hara, Tetsu; Reichl, Brandon G.; D'Asaro, Eric A.; Harcourt, Ramsey R.; Sullivan, Peter P. (2015). "Langmuir turbulence under Hurricane Gustav (2008)." Journal of Physical Oceanography, 45(3): 657-677.
Available at: http://dx.doi.org/10.1175/JPO-D-14-0030.1

Langmuir Turbulence under Hurricane Gustav (2008)

Authors

Tyler J. Rabe, Tobias Kukulka, Isaac Ginis, Tetsu Hara, Brandon G. Reichl, Eric A. D'Asaro, Ramsey R. Harcourt, and Peter Sullivan

Langmuir Turbulence under Hurricane Gustav (2008)

TYLER J. RABE AND TOBIAS KUKULKA

University of Delaware, Newark, Delaware

ISAAC GINIS, TETSU HARA, AND BRANDON G. REICHL

University of Rhode Island, Narragansett, Rhode Island

ERIC A. D'ASARO AND RAMSEY R. HARCOURT

University of Washington, Seattle, Washington

PETER P. SULLIVAN

National Center for Atmospheric Research, Boulder, Colorado

(Manuscript received 20 February 2014, in final form 6 October 2014)

ABSTRACT

Extreme winds and complex wave fields drive upper-ocean turbulence in tropical cyclone conditions. Motivated by Lagrangian float observations of bulk vertical velocity variance (VVV) under Hurricane Gustav (2008), upper-ocean turbulence is investigated based on large-eddy simulation (LES) of the wave-averaged Navier–Stokes equations. To realistically capture wind- and wave-driven Langmuir turbulence (LT), the LES model imposes the Stokes drift vector from spectral wave simulations; both the LES and wave model are forced by the NOAA Hurricane Research Division (HRD) surface wind analysis product. Results strongly suggest that without LT effects simulated VVV underestimates the observed VVV. LT increases the VVV, indicating that it plays a significant role in upper-ocean turbulence dynamics. Consistent with observations, the LES predicts a suppression of VVV near the hurricane eye due to wind-wave misalignment. However, this decrease is weaker and of shorter duration than that observed, potentially due to large-scale horizontal advection not present in the LES. Both observations and simulations are consistent with a highly variable upper ocean turbulence field beneath tropical cyclone cores. Bulk VVV, a TKE budget analysis, and anisotropy coefficient (ratio of horizontal to vertical velocity variances) profiles all indicate that LT is suppressed to levels closer to that of shear turbulence (ST) due to misaligned wind and wave fields. VVV approximately scales with the directional surface layer Langmuir number. Such a scaling provides guidance for the development of an upper-ocean boundary layer parameterization that explicitly depends on sea state.

1. Introduction

Over the past few decades, forecasts for tropical cyclone (TC) track have improved significantly with the development of complex numerical models. However, the ability to predict their strength has not progressed as quickly (DeMaria et al. 2013). This is partially because of the incomplete understanding of turbulent upper-ocean mixing. Extreme winds and complex wave fields drive upper-ocean turbulence, which entrains cooler water from the thermocline to induce significant cooling of the sea surface (Price 1981). Cooling, in turn, reduces the heat fluxes that drive tropical cyclones (Bender and Ginis 2000; Emanuel et al. 2004).

Many studies (e.g., Price et al. 1986; Large et al. 1994; Zedler et al. 2002) have investigated the impact of high winds on upper-ocean turbulence using one-dimensional turbulence parameterizations. They focus on the importance of inertially rotating wind stress on mixing at the thermocline. Resonance between the wind and Eulerian currents can amplify the currents and increase the shear at the base of the mixed layer. Typically, there is a rightward bias in entrainment effects because

Corresponding author address: Tobias Kukulka, 211 Robinson Hall, School of Marine Science and Policy, College of Earth, Ocean, and Environment, University of Delaware, Newark, DE 19716.
E-mail: kukulka@udel.edu

DOI: 10.1175/JPO-D-14-0030.1

of this resonance (Price 1981; Skyllingstad et al. 2000). The one-dimensional parameterizations used in these models do not explicitly include the effects of surface gravity waves, which have been shown to play an important role in upper-ocean mixing (McWilliams et al. 1997; Li et al. 2005).

Nonbreaking ocean surface waves influence turbulence through their interaction with the sheared Eulerian currents. Specifically, the phase-averaged effects of surface gravity waves lead to a net drift (Stokes drift) that tilts vertical vorticity into the direction of wave propagation, creating wind-aligned roll vortices called Langmuir circulations (Langmuir 1938). Craik and Leibovich (1976), and later McWilliams et al. (2004), developed the mathematical theory describing Langmuir circulations based on wave current interactions. The spectrum of temporal and spatial scales exhibited by Langmuir circulations has characterized them as a type of turbulence or Langmuir turbulence (LT) (McWilliams et al. 1997). Many studies (e.g., Plueddemann et al. 1996; McWilliams et al. 1997; Li et al. 2005; Kukulka et al. 2009; D'Asaro et al. 2014) have shown that LT is a dominant feature of upper-ocean turbulence. A common model used to study LT is large-eddy simulations (LES), which are based on the Craik–Leibovich equations (Skyllingstad and Denbo 1995; McWilliams et al. 1997).

Traditional LES studies have consisted of simulating turbulence in wind-wave equilibrium conditions utilizing a Stokes drift profile from a monochromatic wave field (e.g., McWilliams et al. 1997; Li et al. 2005; Polton and Belcher 2007). However, in tropical cyclone conditions, wind and wave fields are rapidly changing and both fields can be significantly misaligned. Some LES studies have investigated the effects of inertially rotating winds with prescribed wave fields (Skyllingstad et al. 2000), LT under various wind and wave age equilibrium conditions (Harcourt and D'Asaro 2008), comparison of LES with nonstationary field observations (Kukulka et al. 2009, 2010, 2013), and wind-wave misalignment conditions (Van Roekel et al. 2012). More recently, Sullivan et al. (2012) investigated the importance of LT under a tropical cyclone using a combined approach between a wave and LES model. They found that LT was a dominant feature of the upper ocean with significant spatial and temporal variability. The complex Stokes drift profiles from the spectral wave simulations resulted in significant misalignment between the wind and Stokes drift at various depths, leading to weaker LT on the left side of the storm. The strength of the LT was shown to be highly dependent on the local evolution of the wind and wave state.

Over the past two decades, in situ observations under tropical cyclones have become more frequent with the development of profiling and Lagrangian floats. Air-deployed profiling floats were first developed to investigate the ocean response to tropical cyclone events (Sanford et al. 1987; Shay et al. 1992). More recently, Lagrangian floats have been used to measure vertical velocities, gas concentrations, and mixed layer evolution (D'Asaro et al. 1996; D'Asaro 2003b,a; D'Asaro and McNeil 2007).

In this study, field measurements of mixed layer–averaged (i.e., bulk) vertical velocity variance (VVV) from Lagrangian floats are compared with simulated bulk VVV from an LES model. The modeling procedure will be similar to that of Sullivan et al. (2012) but with wind and wave fields from Hurricane Gustav (2008). The goals of this study are to better understand the importance of LT under tropical cyclones, determine whether or not wind-wave misalignment is a critical factor for the strength of turbulence, and to determine whether turbulence parameterizations need to explicitly incorporate waves.

2. Observations under Hurricane Gustav (2008)

Three Lagrangian floats were deployed on a line ahead of Hurricane Gustav (2008) at approximately 1300 UTC 31 August 2008 by the 53rd Hurricane Hunter squadron of the U.S. Air Force Reserve. The line spanned the storm track (Fig. 1) with one float passing under the maximum wind (float number 50, Peak), one passing under the eye (float number 51, Eye), and one on the far left-hand side of the storm (float number 53, Edge). After release from the air deployment package, each float surfaced and telemetered its position and then made a slow, stepped descent to about 150 m, equilibrating itself to the water and computing its density relative to the water. A profile of dissolved O_2 and N_2 gas was also measured; results from the gas measurements will be reported elsewhere. The floats then profiled to the surface and began a "Lagrangian drift" (D'Asaro 2003a) by yearday 245.1 (0244 UTC 1 September) during which they continuously adjusted their density to match that of the mixed layer water (10–25 m) and opened a drogue to increase their drag. During this time, the floats were repeatedly carried across the actively mixing layer by the turbulent eddies as shown in Figs. 2a–c. At about yearday 245.85, the floats surfaced and obtained another GPS position fix. For the Peak float, velocity profiles measured by an EM-APEX float (Sanford et al. 2011) deployed a few kilometers away was used to interpolate the Lagrangian float position between the fixes. For the Eye and Edge floats, the trajectories of surface drifters deployed nearby were used. At the end of the mission, the floats surfaced and data were retrieved via the Iridium global satellite system. The floats were recovered by a research vessel.

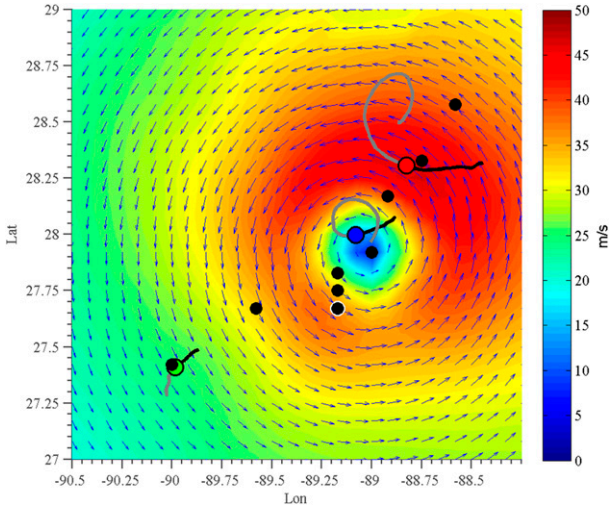

FIG. 1. Wind field for Hurricane Gustav at day 245.27 produced from NOAA H*Wind. Colors represent the magnitude ($m\,s^{-1}$) of the 10-m wind speed ($|\mathbf{U}_{10}|$). Wind vectors are overlaid on the wind magnitude color plot. Wind vectors are scaled relative to the maximum wind. At this time, Gustav is translating at approximately $9\,m\,s^{-1}$ to the northwest. The locations of the three Lagrangian floats are indicated with colored dots with a black outline. The Edge, Eye, and Peak floats are represented in green, blue, and red, respectively. The black/gray lines represent the track of the floats before/after day 245.27. Black dots represent stationary locations. The black dot with a white outline is location 409 that is investigated in detail in section 4d.

Vertical velocity w was computed from the rate of change of pressure for each float. A smoothed vertical velocity variance was computed by filtering w^2 with a fourth-order low-pass Butterworth filter with a half-power period of 9000 s. The resulting smoothed w^2 estimates thus necessarily oscillate at the cutoff frequency of the filter. Float trajectories nearly uniformly fill the upper layer (Fig. 2) so that the average along these trajectories is approximately the layer average of w^2. The large vertical velocities due to surface waves are naturally filtered from these averages because the pressure is constant along the Lagrangian trajectories of surface waves. Vertical lines show 95% confidence limits on w^2. These were computed following D'Asaro (2001), assuming that the correlation time of w^2 is proportional to $(w^2)^{0.5}/h$ where h is the mixed layer depth computed as twice the average value of float depth. The proportionality constant is the same as that in D'Asaro (2001), which assumes that the mixed layer turbulence found in that data has similar statistical properties.

Buoyancy of the floats induces errors in the measurement of w^2 (Harcourt and D'Asaro 2010). The resulting vertical motion of the float relative to the water changes both the measured vertical velocity and causes the mixed layer to be nonuniformly sampled. D'Asaro et al. (2014) find vertical velocities relative to the water of a few millimeters per second for carefully calibrated floats. Errors in float ballasting are likely to be larger here, with a firm upper bound of $0.01\,m\,s^{-1}$. This yields an error of about 16% in the average w^2. The finite size of the float also introduces errors by averaging smaller turbulent eddies. We estimate this error by fitting a universal spectral form to the vertical velocity spectrum for each drift and removing the component due to finite float size (D'Asaro et al. 2014, their supplementary material 4.2.5). The resulting correction ranges from 1.2 to 1.31. Accordingly, all estimates of average w^2 are multiplied by a factor of 1.3. During the passage of the Eye float, there is a dramatic decrease in the vertical velocity; the factor of 1.3 is certainly low during this time, but this is a minor correction to a large effect.

Figure 2d displays the observed bulk VVV from the three floats (thick lines) and the corresponding value for u_*^2 (dashed lines). For the Edge and Peak floats, the bulk VVV roughly tracks with u_*^2. However, the Eye float does not track with u_*^2 after the eye of Hurricane passes over the float. In particular, the Eye float hardly moves at all after the eye passage, rising at about $4\,mm\,s^{-1}$ from 15 to the surface. When it reaches the surface, it remains within 2 m of the surface for 2500 s. In contrast, the peak float moves across the 25-m-deep mixing layer roughly 10 times in the same period. Thus, although u_*^2 are roughly the same at day 245.35 for the Peak and Eye floats, their behaviors are radically different with the Peak float showing strong turbulent mixing and the Eye float showing very little mixing. The differences between the Eye and Peak VVV far exceed the estimated 95% confidence limits. The turbulence in the boundary layer is thus strongly suppressed behind the eye, as is reflected in the dramatic reduction in bulk VVV. The mechanism for this suppression is investigated by comparing these bulk VVV measurements with results from large-eddy simulations.

3. Large-eddy simulations under Hurricane Gustav (2008)

To model the upper-ocean turbulence observed by the three Lagrangian floats, an LES model was used in concert with a wave model similar to the approach by Sullivan et al. (2012). Unlike any previous approaches, the LES and wave models are forced with a NOAA wind product to realistically capture the wind and wave field of Hurricane Gustav (2008).

a. *LES model*

Large-eddy simulations rely on the assumption that small-scale turbulence generally obeys some

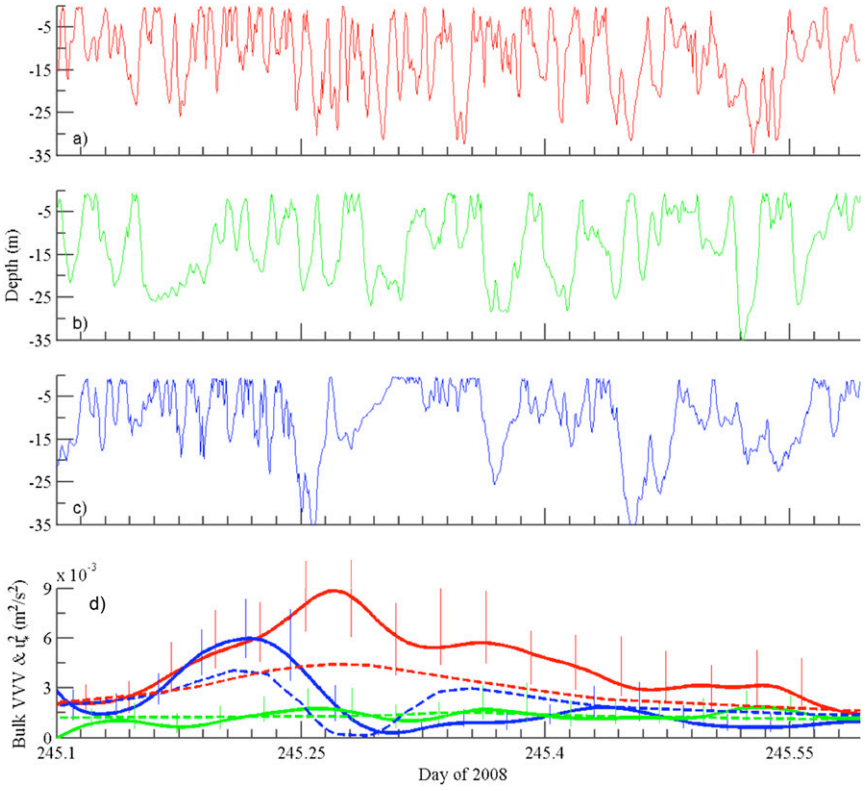

FIG. 2. Depth/time trajectories for the three floats (a) Peak (red), (b) Edge (green), and (c) Eye (blue). Observed bulk VVV with error bars (d) for the Edge (green), Eye (blue), and Peak (red) floats (cf. to float locations in previous figures). The thick lines are the observations and the dashed lines are the wind stress divided by the density $\tau/\rho = u_*^2$. The thin vertical lines represent 95% confidence intervals.

universal characteristics that can be parameterized. LES models are able to resolve the large-scale, energy-containing, turbulent motion while avoiding the extremely high computational cost of resolving the small dissipation-scale eddies. The LES model filters out the subgrid eddies and parameterizes these eddies based on the universal characteristics of turbulence in the inertial subrange. The governing LES equations, based on the equations by Craik and Leibovich (1976), for the resolved scale motion are (McWilliams et al. 1997)

$$\frac{\partial \overline{u}_i}{\partial t} + \epsilon_{ijk}\overline{\omega}_j\overline{u}_k + \epsilon_{ijk}f_j(\overline{u}_k + u_{s,k}) = -\frac{\partial \overline{\pi}}{\partial x_i} + \frac{\overline{\rho}}{\rho_o}g_i + \epsilon_{ijk}u_{s,j}\overline{\omega}_k + \frac{\partial \tau_{ij}}{\partial x_j}, \quad (1)$$

$$\frac{\partial \overline{\rho}}{\partial t} + (\overline{u}_j + u_{s,j})\frac{\partial \overline{\rho}}{\partial x_j} = \frac{\partial \tau_{\rho j}}{\partial x_j}, \quad \text{and} \quad (2)$$

$$\frac{\partial \overline{u}_i}{\partial x_i} = 0, \quad (3)$$

where the rotational form of the nonlinear advective term in the momentum equation is used. All terms with an overbar denote resolved variables (i.e., filtered over the grid scale).

The index $i = (1, 2, 3)$ represents the three coordinate directions (x, y, z), where x is east, y is north, and z is upward. The velocity vector (u, v, w) corresponds to the indexed velocity components (u_1, u_2, u_3). The Coriolis vector $(f_1, f_2, f_3) = (0, 0, f)$, where f is the Coriolis parameter corresponding to a particular latitude. The gravitational acceleration vector is given by $(g_1, g_2, g_3) = (0, 0, -g)$, where $g = 9.81\,\mathrm{m\,s^{-2}}$. The vorticity $\overline{\omega}_i$ is equal to $\epsilon_{ijk}\partial\overline{u}_k/\partial x_j$, where ϵ_{ijk} is the Levi–Civita permutation tensor. The Stokes drift vector is $(u_{s,1}, u_{s,2}, u_{s,3}) = (u_s, v_s, 0)$. The pressure term $\overline{\pi} = (p/\rho_0) + 0.5[(\overline{u}_i + u_{s,i})(\overline{u}_i + u_{s,i})]$ is a generalized pressure that includes the kinetic energy, which appears when the nonlinear advective term is written in rotational form. To capture buoyancy effects, the Boussinesq approximation was used with a constant reference density of ρ_0. Density and temperature are linearly related through the thermal expansion coefficient

$$\alpha = -\frac{1}{\rho}\left(\frac{\partial \rho}{\partial T}\right). \quad (4)$$

A constant thermal expansion coefficient of $\alpha = 2 \times 10^{-4}\,\mathrm{K}^{-1}$ is used. In reality, seawater density is a function of temperature and salinity. As a simplification, the temperature and salinity effects have been combined based on the expansion coefficients and typical temperature and salinity ranges.

The subgrid-scale stresses for momentum and density are τ_{ij} and $\tau_{\rho j}$, respectively. The subgrid-scale fluxes are parameterized via eddy viscosities for both momentum and temperature (i.e., ν_M and ν_T). The subgrid-scale model is explained in detail in the appendix.

Langmuir circulation dynamics are captured through the Stokes drift vorticity interaction term $\mathbf{u}_s \times \overline{\boldsymbol{\omega}}$. The irrotational shear generated by the surface waves acts to tilt vertical vorticity perturbations into the Stokes drift propagation direction. This leads to a series of coherent counterrotating vortices that align roughly with the wind (McWilliams et al. 1997).

b. Surface fluxes

The primary forcing for both the LES model and the wave model is the 10-m atmospheric winds. NOAA's Hurricane Research Division (HRD) has developed a product available for hurricane forecasters that enables them to obtain realistic wind fields in near–real time. This product is widely used by the science and engineering communities (Powell et al. 1998). It is referred to as H*Wind or HRD Wind. The H*Wind project recreates a wind field from a particular tropical cyclone using all available observational data. This includes satellite data, dropsondes, buoy measurements, and measurements from hurricane eyewall–penetrating flights. The result is a composite wind velocity at 10-m height. The wind fields are available at 3-h intervals throughout a tropical cyclones translation. To use the H*Wind predictions, the wind fields are linearly interpolated between ''known'' wind fields to provide constant realistic forcing for the wave and LES models. A full description of the H*Wind product is described by Powell et al. (1998), and an example of a wind field reconstruction, using H*Wind, from Hurricane Katrina can be seen in Powell et al. (2010).

The driving mechanism for the LES model is the surface momentum flux. The surface momentum flux is parameterized via the bulk formula

$$\tau = \rho_a C_d \mathbf{U}_{10} |\mathbf{U}_{10}|, \quad (5)$$

where ρ_a is the air density, and $\mathbf{U}_{10}$ is the two-component wind vector referenced to 10-m height. For moderate winds below $20\,\mathrm{m\,s^{-1}}$, the drag coefficient C_d is parameterized using the formulation from Large and Pond (1981), where

$$C_d = \begin{cases} 0.0012 & |\mathbf{U}_{10}| < 11\,\mathrm{m\,s^{-1}} \\ (0.49 + 0.065|\mathbf{U}_{10}|) \times 10^{-3} & 11\,\mathrm{m\,s^{-1}} < |\mathbf{U}_{10}| < 25\,\mathrm{m\,s^{-1}} \end{cases}. \quad (6)$$

In high wind and misaligned wind and wave conditions, the air–sea momentum flux mechanisms are incompletely understood, and the drag coefficient is not well constrained (Powell et al. 2003; Donelan et al. 2004; French et al. 2007; Sanford et al. 2011; Holthuijsen et al. 2012). Following Sullivan et al. (2012), the drag coefficient is saturated at $C_d = 1.8 \times 10^{-3}$ above wind speeds of $20\,\mathrm{m\,s^{-1}}$. Field and laboratory studies by Powell et al. (2003), Donelan et al. (2004), and French et al. (2007) have shown that for very high wind speeds, the drag coefficient reaches a saturated value. Donelan et al. (2004) showed that this saturated drag coefficient was approximately 2.3×10^{-3}, and an ocean momentum budget analysis from Sanford et al. (2011) showed a lower value of 1.4×10^{-3}. More recently, Holthuijsen et al. (2012) investigated the effects of wind-wave misalignment on the drag coefficient. They showed that the orientation of the wind and the swell waves can influence the drag coefficient significantly.

For all simulations, a dynamically insignificant constant surface cooling of $-5\,\mathrm{W\,m^{-2}}$ is imposed to facilitate the turbulence spinup from rest (McWilliams et al. 1997). The air–sea heat flux during Hurricane Gustav (2008) is likely larger than $-5\,\mathrm{W\,m^{-2}}$; however, surface heat fluxes contribute little to the overall cooling of the mixed layer and to mixed layer turbulence generation under tropical cyclones. Surface heat fluxes likely play a minor role in driving upper-ocean turbulence because the Langmuir stability length $L_L = B_s/(u_*^2 u_s/h)$ is generally much larger than h (Belcher et al. 2012) for typical forcing conditions, even under the hurricane eye (B_s is the surface buoyancy flux). Even imposing a significantly larger surface cooling of $-1000\,\mathrm{W\,m^{-2}}$ results in a ratio of $h/L_L < 0.1$, further supporting that buoyancy forcing is a secondary factor. The primary mechanism by which the mixed layer is

cooled is entrainment of cooler water from the base of the mixed layer, accounting for over 90% of the total cooling (Price 1981; Sullivan et al. 2012).

c. Wave forcing

To generate time-dependent wave spectra a third generation wave model is deployed, WAVEWATCH III (WW3) (Tolman 2009), which has been modified previously to better match with observed hurricane wave fields (Fan et al. 2009). WW3 solves the spectral wave action equation for the directional frequency spectra [i.e., $F(\omega, \theta)$, where omega is the wave frequency and theta denotes the wave propagation direction]. The model accounts for wave dissipation due to whitecapping, wave bottom interactions, nonlinear wave–wave interactions, and wind input, which is driven by H*Wind.

The wave model domain spans from 18° to 31°N in latitude and from 98° to 80°W in longitude to encompass the area with the Lagrangian float observations (Fig. 1). The latitude and longitude are spaced by ½° in each direction to adequately capture the highly variables changes around the eye of the storm.

The wave spectrum in the model is discretized into 24 direction and 40 intrinsic or relative frequencies. The direction is linearly spaced from 0 to 2π. The frequencies span from 0.0285 to 1.1726 Hz with a logarithmic spacing of $f_{n+1} = 1.1f_n$, where n is the nth frequency. The intrinsic frequency is related to the wavenumber through the dispersion relation for deep-water waves. Above a frequency of 1.1726 Hz, an empirical spectral tail, which decays with a slope of k^{-4}, is applied to account for short waves that are not resolved by the model. The spectral tail accounts for an additional 22 frequencies, resulting in 62 total frequencies.

The wind forcing from H*Wind is interpolated using "normalized interpolations" (Fan et al. 2009) between the 3-h spaced H*Wind wind fields to obtain the 30-min wind fields. The wave simulation uses a time step of 300 s. This transient wind field then drives the wave model and produces the time- and space-dependent wave spectrum $F(\omega, \theta)$. The wave spectra are then used to calculate the Stokes drift profiles via

$$\mathbf{u_s}(z) = 2\int_0^\infty \int_{-\pi}^{\pi} \mathbf{k}\omega F(\omega,\theta) e^{2|\mathbf{k}|z}\, d\theta\, d\omega, \qquad (7)$$

which is from Kenyon (1969).

To match the dynamic time step of the LES model to the fixed time step for the Stokes drift profiles and wind forcing, a simple linear interpolation is used.

d. LES setup

For all simulations, a domain of $(L_x, L_y, L_z) = (300, 300, 120)$ m is used with a total of $(N_x, N_y, N_z) = (256, 256, 228)$ grid points. This corresponds to horizontal resolutions Δx and Δy of 1.17 m, and a vertical resolution Δz of 0.52 m with a grid anisotropy ratio of 2.23. Sensitivity tests of grid resolution and domain size have shown that the chosen configuration adequately captures the turbulence.

The initial upper-ocean density structure for the simulations is determined from in situ measurements. The three Lagrangian floats were designed with a vertical profiling mode to allow them to measure the ocean state before and after the storm passes. Before the floats were in Lagrangian drift mode (days 245.1 to 245.6), they were able to take vertical profiles of salinity, temperature, and various gas concentrations. Figure 3 shows the initial potential density profiles (solid) from the three floats as well as the initial profiles used for the Lagrangian float simulations (dashed) that are used as initial conditions. The mixed layer and density gradient are estimated based on the observations.

To initialize the transient simulations, first stationary simulations are generated for each individual case. Each simulation is run with the wind, wave, and initial density profiles for multiple eddy turnover times (h/u_*) or until stationary turbulent statistics are reached. The mixed layer depth h is defined as the depth of the maximum density gradient. At this point, the turbulent fields from the stationary simulations are used to initialize the transient simulations. This includes the fields of velocity, temperature, generalized pressure, and subgrid-scale (SGS) turbulent kinetic energy. The time-varying wind and Stokes drift profiles are applied to the LES simulations to force the turbulence. The simulations are run for approximately 12 physical hours for the Lagrangian floats simulations and 37 physical hours for the stationary locations. To examine the importance of the wave field on the turbulence in the upper ocean, simulations are run with and without the Stokes drift. These cases will be referred to as Langmuir turbulence (LT) and shear turbulence (ST), respectively.

e. Simulated locations

Study locations were chosen perpendicular to the translation direction of Gustav to best understand the spatial variability of the turbulence across the track of Gustav. Gustav passed from the southeast to the northwest (Fig. 1). Nine stationary locations and three Lagrangian float "locations" are chosen (Fig. 1). To simulate the turbulence at each stationary location, local wind and wave forcing is imposed.

To determine space- and time-dependent forcing conditions for the Lagrangian floats, we interpolate the wind and wave forcing depending on the float location. This provides realistic forcing that each of the floats were experiencing as they drifted with the mean currents. The interpolated 10-m wind speed, the significant wave

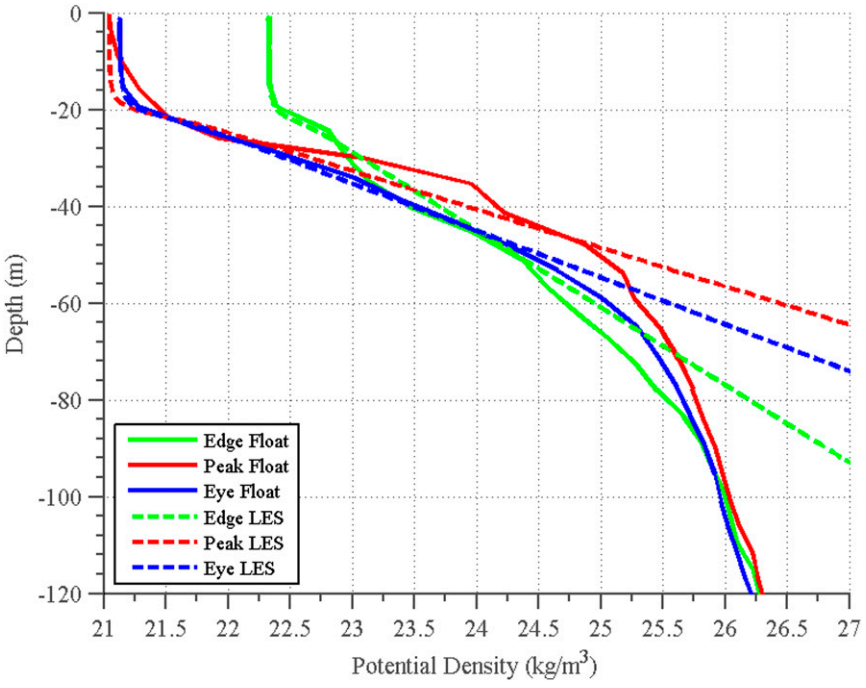

FIG. 3. Potential density profiles for the three floats (solid) and the initial density profiles used in the LES model (dashed). Profiles were taken at day 245.083.

height, and the wind direction for the Edge (green), Eye (blue), and Peak (red) floats are displayed in Fig. 4. The misalignment angle θ_{ww} between the wind direction and the Stokes drift direction at various depths,

$$\cos[\theta_{ww}(t,z)] = \frac{\mathbf{U}_{10}(t)\cdot\mathbf{u}_s(t,z)}{|\mathbf{U}_{10}(t)||\mathbf{u}_s(t,z)|}, \tag{8}$$

highlights the directional variability in the Stokes drift profile with depth (Fig. 5).

The Edge float (Fig. 4, green), to the left of Gustav's eye, experiences relatively constant wind forcing throughout the Lagrangian measurement period (days 245.1 to 245.6). Throughout this time, the wind direction at the Edge float changed by 90°. The significant wave

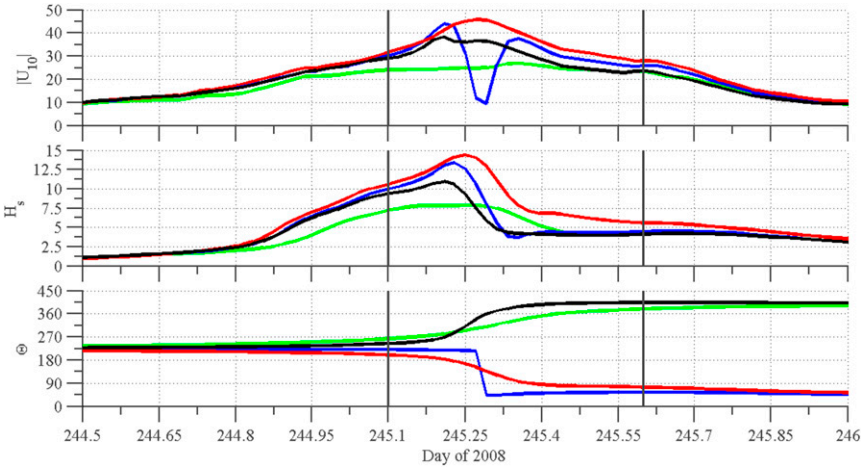

FIG. 4. Forcing conditions for the three Lagrangian floats and location 409: (top) the magnitude of the 10-m wind speed, (middle) the significant wave height, and (bottom) the wind direction. The wind direction is oriented in the traditional x–y space with 0° being east. The Edge, Eye, and Peak floats are represented in green, blue, and red. Location 409 is represented in black. The vertical gray lines indicate the float measurement period from days 245.1 to 245.6.

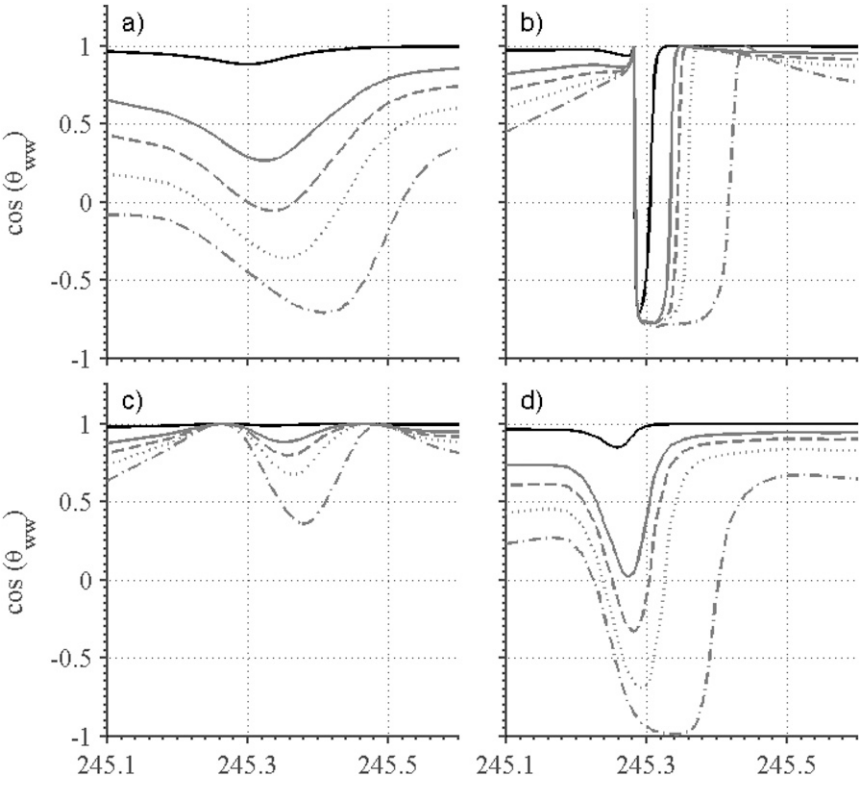

FIG. 5. Misalignment angle between the wind and the Stokes drift given by Eq. (8) for the (a) Edge float, (b) the Eye float, (c) the Peak float, and (d) location 409. The misalignment angle is shown at the surface (black) and at depths z = (4.74, 10, 19.47, and 59.47) m (gray: solid, dash, dotted, and dashed–dotted). The misalignment is shown over the period of days 245.1 to 245.6.

height, related to the strength of the Stokes drift, changes from 7.5 to below 5 m when the wind direction is shifting. Figure 5a shows that the shift in wind direction causes the Stokes drift profiles to become misaligned with the wind. The Eye float (Fig. 4, blue) experiences the most variable forcing conditions. The wind speed reaches a peak around 45 m s^{-1} and has a rapid reduction around day 245.25, followed shortly by an increase in the wind speed. This is due to the hurricane translating over the float and the float moving directly into the hurricane eye (Fig. 1). As the wind speed is rapidly changing, the wind direction is also shifting by 180°. These rapidly changing conditions have strong effects on the significant wave height, which changes from 12.5 m at day 245.2 to 5 m around day 245.3. These changes cause the Stokes drift profiles to become almost 180° misaligned with the winds (Fig. 5b). The Peak float experiences very consistent strong forcing throughout the 12-h observation period as indicated in Fig. 4 (red). The wind speed reaches approximately 50 m s^{-1}, and the significant wave height reaches 15 m. The wind direction changes slowly by approximately 90°. As seen at the Edge and Eye float, the significant wave height has a rapid drop-off as the storm passes over the Peak float. However, the Stokes drift profiles remain relatively aligned with the wind direction (Fig. 5c). Note that for some locations the wind speed remains relatively constant, but the wind and wave misalignment significantly changes [e.g., station 409; compare forcing in Fig. 4 (black curves) with Fig. 5d].

4. Results

a. *Comparison with observations: Sea surface density and temperature*

Sea surface density changes, which in this study are mainly driven by salinity changes, are estimated from the float observations in the upper 5 m and compared to simulations [top panels Fig. 6, observations are dots, LES is black (LT) and gray (ST) lines]. As anticipated, the largest surface density changes occur for the resonant peak float location, and the weakest occur for the off-resonant edge float location. Overall, simulations and observations agree surprisingly well, given the complexities of the tropical cyclone system discussed below. For the eye float location, small surface density

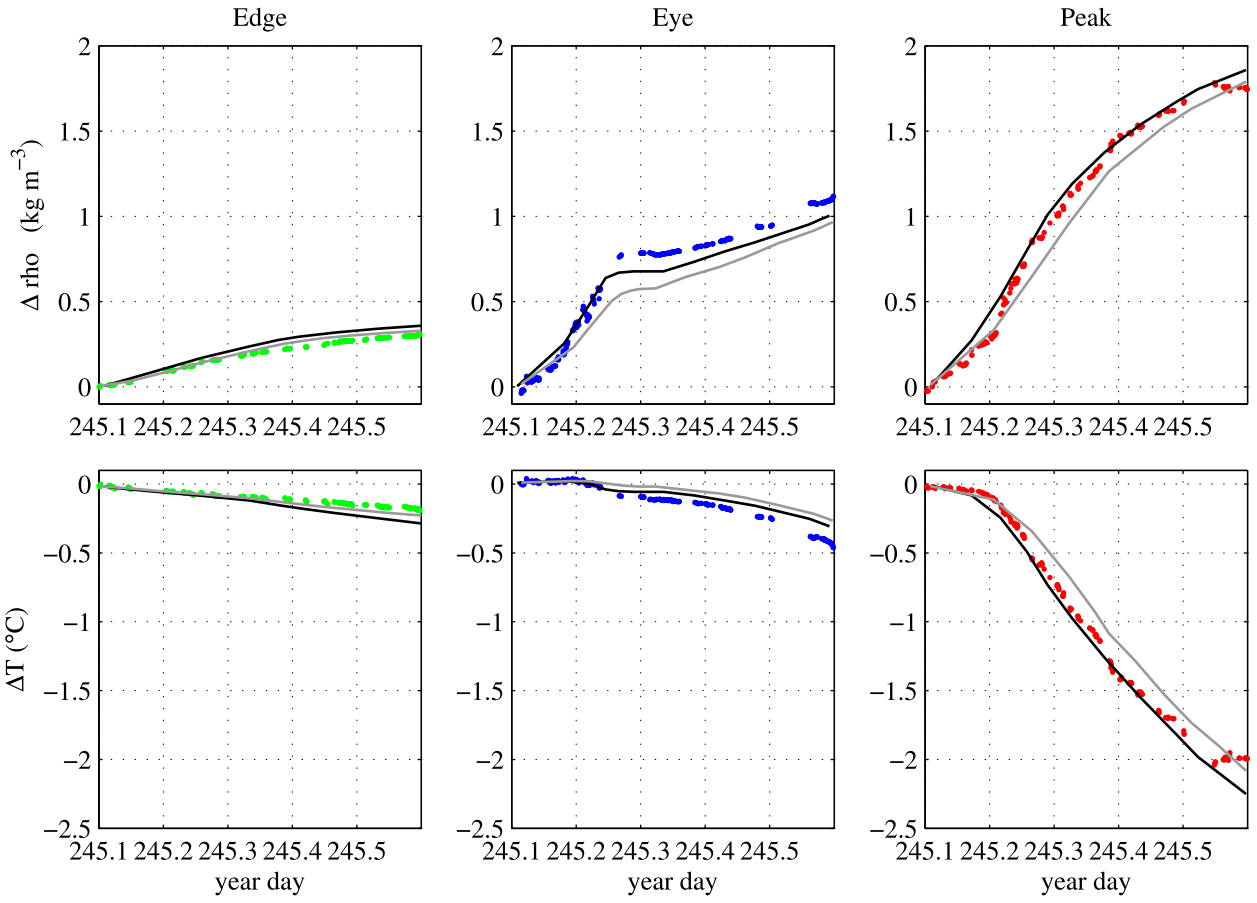

FIG. 6. (top) Sea surface density changes ($\Delta\rho$) and (bottom) sea surface temperature changes (ΔT) for the (left) Edge, (middle) Eye, and (right) Peak float locations; observations (dots) and simulations (solid lines) with LT (black) and without LT (gray).

changes during the passing of the eye with low wind conditions are captured in both observations and simulations. LES results with LT agree better for the peak and eye float locations, whereas the LES result without LT agrees better at the edge location, where the LT effect is relatively small anyways. However, a detailed comparison between observations and LES is nontrivial because of the uncertainties in the drag coefficient outlined below.

It is also interesting to compare our simulations to observed changes in sea surface temperature (ΔT, bottom panels, Fig. 6). Since we only model density in our simulations, temperature changes are estimated based on the observed density–temperature relationship. Therefore, LES results show a similar trend as discussed for the sea surface density change and also agree reasonably with observations. Note that LES results are consistent with the observed maximum sea surface cooling of 2°C at the peak location (right bottom panel of Fig. 6). Sea surface temperature cooling can be enhanced by more than 0.3°C by LT while the SST cooling event is taking place, which may have a significant impact on TC development.

b. *Comparison with observations: VVV*

To further assess the model performance, mixed layer–averaged VVV, which plays a key role in vertical mixing and transport, is compared with observations. In particular, the importance of LT during tropical cyclones is assessed, and the effects of wind and wave misalignment on the suppression of turbulence are investigated.

The total, that is, resolved plus unresolved SGS contributions, LES bulk VVV is calculated via

$$\langle w_T'^2\rangle_h = \frac{1}{h}\int_{-h}^{0}\left(\langle\overline{w}^2\rangle + \langle w_{\mathrm{SGS}}'^2\rangle\right)dz, \qquad (9)$$

where h is the mixed layer depth, and subscript T represents total VVV including the subgrid-scale VVV. The subgrid-scale VVV is calculated under the assumption of isotropic turbulence. It is defined as $w_{\mathrm{SGS}}^2 = 2/3e$,

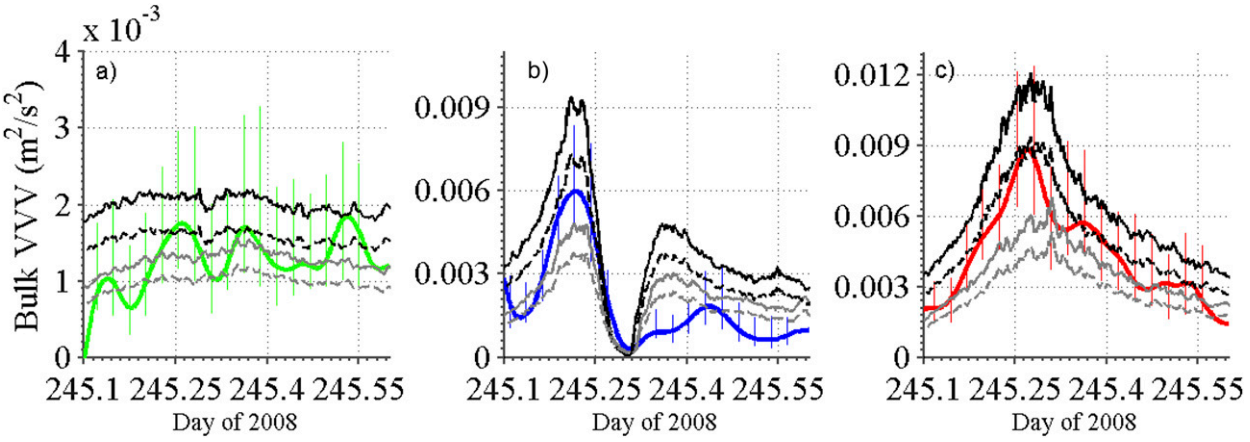

FIG. 7. Bulk VVV comparison between simulations and observations for the (a) Edge, (b) Eye, and (c) Peak floats. The green, blue, and red lines are the observations (including error bars), the solid black lines are the LES results for LT, and the solid gray lines are the LES results for ST. The dashed black/gray lines are estimated VVV based on a lower saturated drag coefficient of $C_d = 0.0014$. The thin vertical lines represent 95% confidence intervals.

where e is the subgrid-scale turbulent kinetic energy (TKE). Angle brackets indicate horizontally averaged quantities from the three-dimensional LES output.

For the Edge float, the observed bulk VVV (green) falls between the simulation results for LT (solid black) and ST (solid gray) (Fig. 7a). There is considerable variability in the observations, spanning between the simulation results for LT and ST. Relatively constant bulk VVV levels are expected at this location because the wind speed is almost constant and only turns gradually (green curves Fig. 4). The variability in the LT simulation results is generally influenced by the strength of the Stokes drift profile [inferred from significant wave height in Fig. 4 (green)]. The misalignment between the wind and the Stokes drift only changes gradually and thus does not drive the variability for the LT simulations (Fig. 5a).

The Eye float experiences the most variable forcing conditions (blue lines Fig. 4), and, accordingly, VVV levels are also highly variable (Fig. 7b). Before the eye of the storm passes over the float, the observed bulk VVV level falls in between the levels predicted with the shear and LT simulations. However, as the storm's eye passes over the float around day 245.3, the observed bulk VVV suddenly falls below the levels predicted by both the ST and LT simulations and remains low for the rest of the measurement period. The simulations capture a suppression of turbulence, but it is not as strong or as long as observed.

Figure 8 shows the Eye float data in more detail. Before day 245.28, turbulent eddies repeatedly carry the float across the mixed layer (Figs. 2b, 8a) and into the underlying stratification. The float measures active entrainment at the bottom of the mixed layer; its density increases below 25 m (Fig. 8b, blue), and the water coming up is heavier than the water going down (D'Asaro 2003a). A similar pattern resumes after day 245.36 (Fig. 8b, red). Between these times, the strong mixing stops and the float drifts upward to the surface at a nearly steady speed of $7\,\mathrm{mm\,s^{-1}}$ with little change in density. This indicates a nearly complete absence of turbulent mixing; the upward drift is most likely because of a slight misballasting of the float. From days 245.31 to 245.36 (Fig. 8, green to orange), the float's vertical kinetic energy and depth of mixing slowly increase, but with no evidence of vertical entrainment. It thus appears that the strong suppression of turbulence during and after the eye passage is not due to stratification, and therefore must be due to another effect.

The Peak float experiences very consistent strong wind and wave forcing throughout the 12-h observation period (Fig. 4, red lines). Similar to the Edge float results, the observed bulk VVV (red) falls in between the LT (solid black) and ST (solid gray) (Fig. 7c).

The observations and LES comparisons of bulk VVV reveal three important insights on upper-ocean turbulence under tropical cyclones. First, overall (except for the Eye float after day 245.3) the observed bulk VVV for all three floats falls in between the Langmuir and shear LES results. This suggests that LT is important during tropical cyclones. Although there is considerable variability in the measurements, the observed, elevated VVV cannot be obtained without the addition of the Craik–Leibovich vortex force. Second, the simulations for LT systematically overpredict the observations, which may be because of incorrect parameterizations of the drag coefficients in high winds and complex seas. Third, although the simulations capture significant suppression of turbulence due to surface waves (discussed below), it is unlikely that LT alone caused the strong

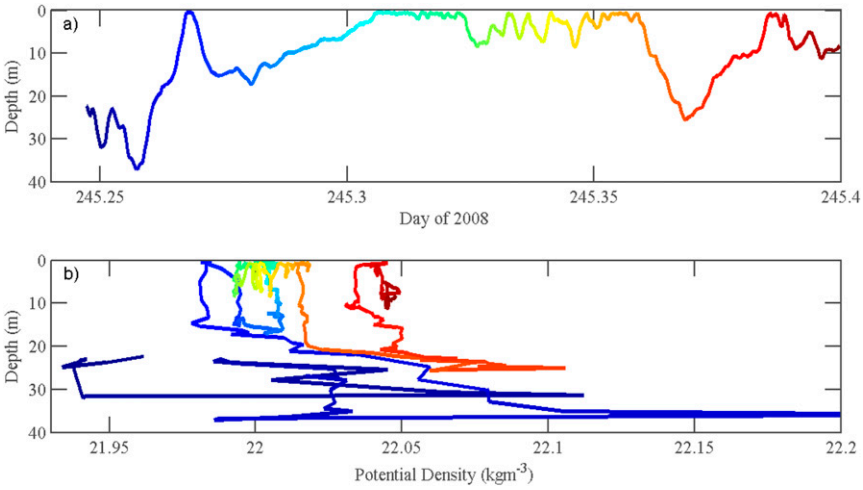

FIG. 8. Detail of Eye float during eye passage. (a) Depth colored by time. (b) Potential density against depth colored by time.

suppression of turbulence measured by the Eye float after day 245.3.

c. *Modeling uncertainties*

1) BASIC WAVE AND LES APPROACH

Modeling uncertainties are associated with wave field predictions and the LES model assumptions. The wave model, based on the wave action equation, makes approximations for wave action source terms. Wave input and wave dissipation are not well understood in complex wind conditions typical of tropical cyclones. Nevertheless, the wave model has been tested previously in hurricane conditions (e.g., Fan et al. 2009) and results agree with observations. Therefore, wave field uncertainty is unlikely to play a significant role in the errors. The LES model employs a subgrid-scale model with turbulence closure assumptions. However, the solution to the LES equations is likely insensitive to the subgrid parameterization because the turbulence is well resolved (greater than 85%) (Pope 2000). Domain size and grid resolution also play an important role in the solutions accuracy. However, sensitivity tests revealed that a large domain size and higher spatial resolution do not significantly change the results presented here.

2) BREAKING WAVES

Breaking waves, which inject TKE near the ocean surface (Melville 1996; Terray et al. 1996), are not explicitly captured in the modeling approach. Previous observational studies (e.g., Terray et al. 1996) for wind-wave equilibrium conditions indicate that the breaking wave effect is mainly confined to the surface and does not significantly influence the bulk mixed layer dynamics that is the focus of this study. LES studies by Noh et al. (2004) and Sullivan et al. (2007) suggest that breaking waves may interrupt Langmuir circulation structure close to the surface, but do not strongly influence bulk VVV. Finally, it is theoretically not well understood how to include stochastic wave breaking events in the Craik–Leibovich equations, which have been originally derived for turbulent motion that is significantly weaker and slower than the motion of breaking waves. Clearly, the breaking wave effect is an important unknown that needs to be addressed in future studies.

When the ocean restratifies under the eye (see discussion below), the mixed layer shoals and potentially becomes comparable in depth to the significant wave height of approximately 5 m (Fig. 4, blue line, center). If breaking wave effects penetrate roughly to a depth consistent with the significant wave height, this could significantly disrupt LT structure and reduce the bulk VVV. It is important to note that only part of the wave spectrum, which is actively forced by the wind, contributes to breaking waves and thus the penetration depth is likely less than the significant wave height. Furthermore, when the eye passes over the float, the wind speed rapidly increases to above $30\,\mathrm{m\,s^{-1}}$, which likely leads to significant breaking wave events that inject bubbles into the mixed layer. Bubbles have been shown to enhance the near-surface stratification and suppress turbulence (Smith 1998; Gemmrich 2012). These combined effects could lead to reduced bulk VVV levels consistent with observations.

3) THREE-DIMENSIONAL EFFECTS

The LES approach does not capture any lateral effects, such as Ekman pumping or large-scale horizontal

advection. Results of observations and simulations from Sanford et al. (2011) indicate that the ocean restratifies below the eye due to vertical advection of the thermal field likely due to Ekman pumping. If this stratification suppresses upper-ocean turbulence it may contribute to the low VVV levels observed by the Eye float after the passing of the storm.

4) DRAG COEFFICIENT

Finally, the drag coefficient uncertainty in high wind (Powell et al. 2003; Donelan et al. 2004) and complex wave conditions (Holthuijsen et al. 2012) is another important factor influencing the differences between the observed and simulated bulk VVV. Recent analysis of ocean momentum budgets have indicated that the drag coefficient C_d under tropical cyclones with wind speeds from 30 to 47 m s^{-1} is approximately 1.4×10^{-3} (Sanford et al. 2011). Holthuijsen et al. (2012) describe a large range in drag coefficient, based on an analysis of boundary layer wind profiles. They found that the orientation of the wind and the swell waves can reduce the drag coefficient to 1×10^{-4}, that is, smaller than the value used in this study. Assuming that the bulk VVV is proportional to the wind stress, the drag coefficient can be estimated from the simulations. Using $C_d = 0.0014$ from Sanford et al. (2011) to scale our previous results, estimated simulated bulk VVV reduces (dashed black/gray lines in Fig. 7). Note that for this simple rough scaling estimate, we do not change the wave fields or rerun the LES. The LT simulations (dashed black) agree well with observations suggesting that the drag coefficient at wind speeds above 30 m s^{-1} may be less than the chosen saturated value of 0.0018. Although the simulations results agree much better with the observations with a lower drag coefficient, the suppression observed by the Eye float is still stronger than a lower drag coefficient can explain. It is likely that the combined effects of the modeling uncertainties could lead to low bulk VVV levels consistent with the observations behind the eye of Gustav. Note also that the buoyancy entrainment, and thus the mixed layer deepening and surface cooling, may be significantly overestimated if the drag coefficient is lower than we estimated. However, relative strength of buoyancy entrainment with and without LT would be similar provided that the turbulent Langmuir number remains approximately the same (Grant and Belcher 2009).

A smaller wind stress estimate should also result in smaller sea surface density changes because of the reduced turbulent buoyancy fluxes at the mixed layer base. A simple scaling correction of sea surface density change for different wind stresses, similar to the scaling of VVV above, is not straightforward to obtain because sea surface density changes evolve dynamically. A key quantity for such scaling relation is the buoyancy entrainment rate, which roughly scales as u_*^3/h; however, the mixed layer depth h itself depends on the history of the buoyancy entrainment, complicating scaling arguments.

Given the aforementioned complexities of the tropical cyclone system and the straightforward approach without any adjustments to enhance the agreement between observations and simulations, the comparison is overall surprisingly good and encouraging. In particular, the results suggest that LT plays a significant role under tropical cyclones and critically influences upper-ocean turbulence variability.

d. *Variability of upper-ocean turbulence under tropical cyclones due to LT*

To further investigate the spatiotemporal variability of the upper-ocean turbulence in response to complex wind and wave conditions, the LES results for the nine fixed locations across the track of Gustav are investigated (Fig. 1). Before presenting the results for all locations, a single location (location 409; Fig. 1) that highlights the strong variability in LT is first investigated.

1) IN-DEPTH ANALYSIS OF A SINGLE LOCATION

Location 409 is located to the left of the eye of Gustav near the radius of maximum winds. This location experiences very consistent wind forcing with highly variable changes in the wave field. The wind speed time series at location 409 is almost symmetric with respect to the time of maximum winds, at which the wind speed is approximately 40 m s^{-1} (Fig. 4). The significant wave height increases as the storm approaches and then quickly subsides, similar to the forcing conditions experienced by the Peak float. The misalignment during this period is relatively strong and persistent (Fig. 5d). Particularly important are the surface misalignment and the misalignment at $z = -4.74$ m that contribute significantly to the Stokes drift shear production term in the TKE budget. As noted earlier, misalignment in the wave field can have drastic impacts on the VVV in the mixed layer through a countergradient production term in the TKE budget (Van Roekel et al. 2012; Sullivan et al. 2012).

To assess the importance of the wave field on the VVV, the VVV (including SGS) normalized by u_*^2 will be investigated. The normalization removes the dependence on the changes in wind stress magnitude and allows for an investigation into the impacts of the wave field and the changing wind direction.

From days 245.1 to 245.6, which is the dynamically interesting time range when the wave field is rapidly

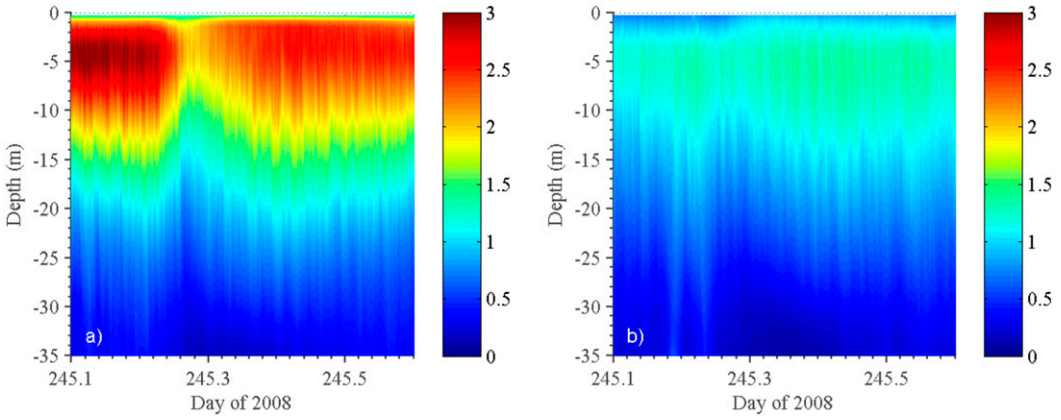

FIG. 9. Normalized VVV (w'^2/u_*^2) for (a) LT and (b) ST cases between days 245.1 and 245.6.

changing, LT has significantly enhanced VVV relative to ST, as expected [LT simulation (Fig. 9a) and ST simulation (Fig. 9b)]. The ST simulation shows relatively consistent normalized VVV levels suggesting a VVV scaling with u_*^2. There is a slight reduction in the normalized ST VVV level around day 245.25. This can be attributed to the changing wind direction, which results in adjusting upper-ocean turbulence (cf. with Fig. 4). The LT simulation, however, shows a drastic reduction in the normalized VVV around day 245.25. This can be attributed to the combined effects of the changing wave field and the misalignment between wind and wave directions.

To assess the magnitude of the changes in normalized VVV and determine the importance of the wave field on the variability of the turbulence, the bulk VVV for the LT simulation is scaled relative to the bulk VVV for the shear simulation (Fig. 10). In spite of significant wind-wave misalignment, waves always enhance VVV. Before day 245.25, the LT bulk VVV is twice that of the ST bulk VVV. As Gustav's eye passes location 409, the wind-wave misalignment changes rapidly (Fig. 5d), so that around day 245.25, the scaled bulk VVV decreases from 2.25 to 1.5 very rapidly. This suggests that turbulence can be suppressed by the effects of the surface gravity waves from strong LT to a near ST regime. This drastic wave-dependent change suggests that upper-ocean turbulence parameterizations employed in TC ocean models need to be dependent on the directional wave field. To capture this significant variability, LT must be considered.

To more fully understand these rapid changes in the bulk VVV seen above, the horizontally averaged TKE budgets for the ST and LT simulations are investigated. This will provide insight into the effects of the changing wave conditions on the turbulence. The horizontally averaged, resolved TKE equation is

$$\frac{\partial(k)}{\partial t} = -\langle u_i' w' \rangle \frac{\partial \langle u_i \rangle}{\partial z} - \langle u_i' w' \rangle \frac{\partial u_{s,i}}{\partial z} + \frac{\langle w' \rho' \rangle}{\rho_0} g - \frac{\partial}{\partial z}\left(\left\langle \frac{1}{2} u_i' u_i' w' \right\rangle + \frac{\langle w' p' \rangle}{\rho_0} \right) - \langle \epsilon \rangle + \mathrm{SGS}, \quad (10)$$

where $k = 1/2\langle u_i' u_i' \rangle$ is the resolved turbulent kinetic energy [for a more complete discussion of TKE budgets, see, e.g., Skyllingstad et al. (2000)]. Each resolved variable can be broken down into a horizontal mean and a deviation from the mean via $\overline{u}_i = \langle u_i \rangle + u_i'$. The angle brackets denote horizontally averaged quantities. The terms in Eq. (10) from left to right are the temporal rate

FIG. 10. Bulk VVV from the LT simulation $\langle w_T'^2 \rangle_h$, see Eq. (9), scaled relative to the bulk VVV from the ST simulation.

of change of resolved turbulent kinetic energy per unit mass (per unit mass will be neglected herein for brevity), resolved TKE Eulerian shear production, Stokes drift shear production, resolved buoyancy flux, vertical gradient of resolved vertical TKE flux, vertical gradient of pressure work, and dissipation. Subgrid-scale terms are denoted as SGS. Since the simulation results are well resolved (approximately 85%), SGS terms are not explicitly included in the budgets. All subgrid-scale budget terms, including TKE dissipation rates, are described in the appendix.

The instantaneous TKE budget will be examined at two specific time points for LT and ST simulations to highlight the differences in the energetics before and during the misalignment of the wave field. The first time point is at day 245.115 when the wind and wave field are relatively well aligned and the wind speed is still increasing (Fig. 4, black line, top). The wind speed is approximately 30 m s^{-1} at this time, and the wind direction has not started to shift (Fig. 4). The second time point is at day 245.285 when the wave field is highly misaligned and the wind direction is shifting (Fig. 4). At this time the wind speed is approximately 35 m s^{-1}.

At day 245.115, the TKE budget for the ST simulation displays a balance between Eulerian mean shear production and dissipation between the surface and $z/h = -0.25$ (Fig. 11b). The divergence of vertical TKE flux also plays a small role near the surface. Below $z/h = -0.25$, the budget is a balance between mean shear production, dissipation, and buoyancy flux. This is consistent with shear-driven boundary layers. In contrast, the LT results in Fig. 11a display three important distinctions from the ST result; the Stokes drift shear production is a dominant term through the upper half of the mixed layer, the Eulerian shear production is small except near the surface and near the mixed layer base, and the budgets are considerably more complex. It is also important to note that the vertical gradient of vertical TKE flux (thin gray line) is significantly enhanced in the LT simulation relative to the ST simulation. This is caused by Langmuir circulations increasing the vertical transport of highly energetic turbulence to the base of the mixed layer. The peak in the Eulerian shear production near the base of the mixed layer is characteristic to LT in relatively shallow ocean surface boundary layers, where LT efficiently transports and homogenizes horizontal momentum throughout the mixed layer to enhance shear locally at the mixed layer base (Kukulka et al. 2010; Grant and Belcher 2011). At day 245.115, LT clearly plays a key role in TKE budgets. Note that the TKE budget terms in the upper mixed layer are consistent with earlier studies (e.g., Grant and Belcher 2009; Kukulka et al. 2010).

In contrast to the TKE budget at day 245.115, at day 245.285, when wind and waves are misaligned, the LT and ST results are more similar to one another (Figs. 11c,d). Below $z/h = -0.25$, both the LT and ST TKE budgets display a dominant balance between mean shear production and dissipation. In the region between $z/h = 0$ to -0.25, the Stokes drift shear production (Fig. 11c) again plays an important role in the TKE budget for the LT simulation. The misalignment in the wave field caused the Stokes drift shear production to decrease significantly. The Stokes drift shear production only penetrates to a depth of $z/h = -0.25$ that is much shallower than the TKE budget displays at day 245.115. The similarity between Figs. 11c and 11d suggests that the LT simulation has transitioned toward a shear-driven turbulence regime because of the misaligned wave field. The Stokes drift shear production in the VKE equation causes the reduction in the VKE; the turbulent fluxes are misaligned with the gradients in the Stokes drift and are essentially a countergradient production (Sullivan et al. 2012). Thus, the transient wave response to a rapidly turning wind field determines the upper-ocean turbulence characteristics under tropical cyclones.

The vertically integrated Stokes drift (black dashed–dotted line) and the Eulerian shear (gray line) production terms highlight the impact of the misaligned wind and wave fields on the TKE production (Fig. 12). Only around day 245.25, when wind and waves are strongly misaligned (cf. with Fig. 5), does the Stokes drift shear production drop below the level of the Eulerian shear production (solid black line). Interestingly, the total TKE production for the simulations without LT (gray lines) exceeds the one for the simulations with LT (line with stars for LT). This is because of enhanced shear (reduced mixing) in the simulations without LT resulting in enhanced surface currents and elevated surface fluxes of mechanical energy.

It is useful to investigate the alongwind, crosswind, and vertical velocity variance profiles to diagnose LT from ST. If the wind blows in the x direction, typical ordering of the variances away from the surface for ST are $\langle u_T'^2\rangle > \langle v_T'^2\rangle > \langle w_T'^2\rangle$ and for LT are $\langle w_T'^2\rangle > \langle u_T'^2\rangle > \langle v_T'^2\rangle$ (McWilliams et al. 1997; Polton and Belcher 2007). Since in the hurricane simulations the wind direction is constantly changing, profiles of the turbulent anisotropy coefficient (Polton and Belcher 2007) are examined, which are defined as

$$R_t = \frac{\langle w_T'^2\rangle}{\langle u_T'^2\rangle + \langle v_T'^2\rangle}. \tag{11}$$

If R_t is 0.5, then the turbulence is isotropic turbulence; if it is less than 0.5, it is shear driven; and if R_t is greater

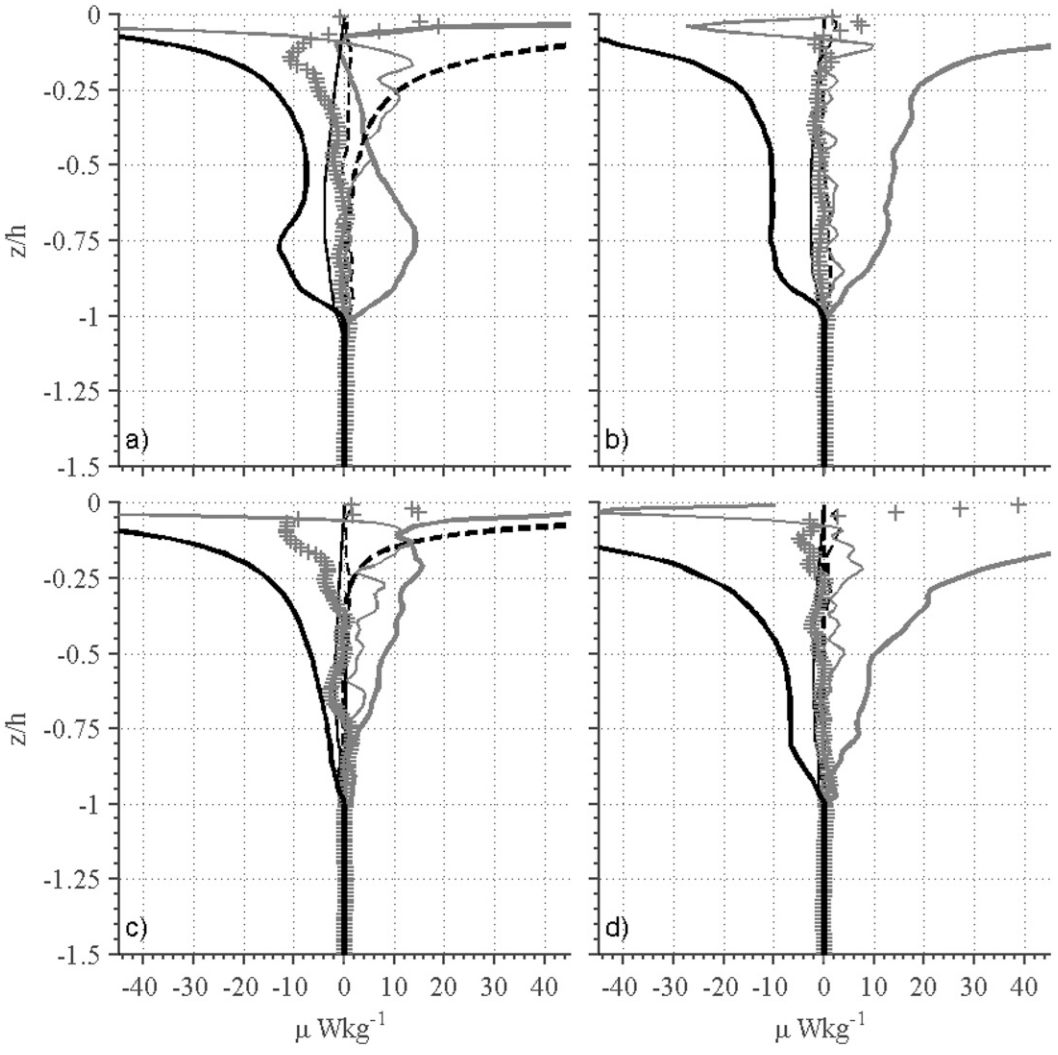

FIG. 11. TKE budget for the (a),(c) LT and (b),(d) ST cases at days (top) 245.115 and (bottom) 245.285. The thin black dashed line represents the time rate of change of total TKE, the thick solid gray line represents the resolved mean shear production, the thick black dashed line [in (a) and (c) only] represents the Stokes drift shear production, the thin solid black line represents the resolved buoyancy production, the thin solid gray line represents the vertical flux of resolved TKE, the pluses represent the vertical pressure work, and the thick solid black line represents the dissipation. Refer to Eq. (10).

than 0.5, the turbulence is Langmuir driven. Figure 13 shows the turbulent anisotropy coefficient for the LT (black curves) and ST (gray curves) simulation results at day 245.115 (solid) and day 245.285 (dashed), corresponding to the TKE budgets in Fig. 11. At day 245.115, the profile indicates very strong LT (solid black) with R_t approaching 0.8 at $z/h = -0.2$. In contrast, the profiles for the ST (solid gray) show values less than 0.2. At day 245.285, the R_t profiles for LT (dashed black) indicate that the turbulence has become more isotropic or shear generated with a peak in R_t of 0.5. The profile for the LT case at day 245.285 (dashed black) still indicates some Langmuir turbulence activity (i.e., subsurface peak around $z/h = -0.1$); however, it is significantly weaker than before. The ST anisotropy profile (dashed gray) for the later time point indicates strong ST with a maximum in R_t of 0.3. This result is consistent with the TKE budget results shown above and confirms that the effects of the misaligned wave field can change the characteristics of the turbulence from a LT regime to a ST regime.

The horizontal cross section of vertical velocity normalized by u_* at the depth of maximum R_t (above $z/h = -0.5$) for the LT and ST simulations supports the TKE budget and R_t profile results that indicate a transition from LT to ST (Fig. 14). Normalized vertical velocities are much more organized and stronger with LT

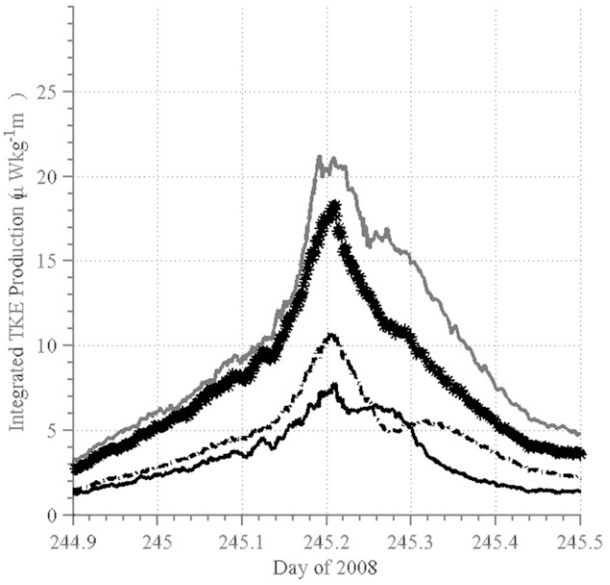

FIG. 12. Vertically integrated production terms for location 409: Eulerian current shear production (solid lines) with LT (black) and without LT (gray), Stokes drift shear production (dashed–dotted line), and total shear production with LT (stars). Note that the TKE budgets shown in Figs. 11a,b and 11c,d correspond to days 245.115 and 245.285, respectively.

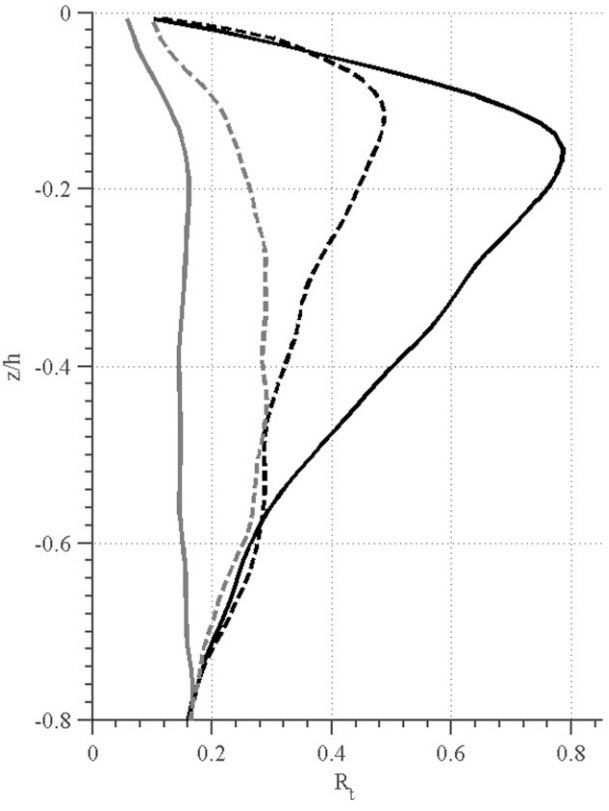

FIG. 13. Turbulent anisotropy coefficient R_t (Polton and Belcher 2007) at day 245.115 (solid lines) and day 245.285 (dashed lines) for the LT (black) and ST (gray) cases.

(left panels) than without (right panels). At day 245.285, the LT (Fig. 14c) and ST (Fig. 14d) contours indicate that the vertical velocities are more similar with significantly weakened LT (Fig. 14c). Although the LT is weakened relative to results from day 25.115 (Fig. 14a), the flow structures in Fig. 14c are more organized than those from day 245.285 without LT (Fig. 14d), indicating that the LT has not fully transitioned to ST, but rather significantly weakened.

The investigation of turbulence characteristics at a single station reveals that, first, LT always enhances VVV levels in the mixed layer relative to ST. Second, the wave field can influence drastic changes in bulk VVV (Figs. 9, 10), especially in close proximity to the eye. Finally, LT simulation results indicate that the characteristics of turbulence can approach those of ST through wind-wave misalignment (Sullivan et al. 2012). Next, the spatial and temporal variability of turbulence across the track of Gustav is investigated by examining all simulated locations.

2) LANGMUIR NUMBER SCALING

To obtain a broader view of the turbulence response of the upper ocean, the results from all nine stationary locations as well as the three float simulations will be investigated. In particular, the interest is in how the turbulent Langmuir number ($\mathrm{La}_t = \sqrt{u_*/|\mathbf{u}_s(0)|}$) affects the normalized bulk VVV. The turbulent Langmuir number has traditionally been used to describe LT and to develop scalings for vertical mixing.

The definition of the surface layer Langmuir number from Van Roekel et al. (2012) and Harcourt and D'Asaro (2008) is utilized here. It incorporates the misalignment between the wind and Stokes drift as well as the Lagrangian shear direction (Sullivan et al. 2012). This modified Langmuir number projects the surface stress and Stokes drift into the Lagrangian shear direction, which has been shown to predict the Langmuir circulation direction by Van Roekel et al. (2012), via

$$\mathrm{La}_{\mathrm{SL}^*} = \sqrt{\frac{u_* \cos(|\alpha_L - \Theta|)}{|\langle \mathbf{u}_s \rangle_{0.2h}| \cos(|\alpha_L - \Theta_S|)}}, \qquad (12)$$

where α_L is the Lagrangian shear direction, Θ_S is the Stokes drift direction, and Θ is the wind direction. Van Roekel et al. (2012) provided some physical motivation for $\mathrm{La}_{\mathrm{SL}^*}$ based on vorticity and TKE budget considerations; however, it is also clear from their discussion that it is not straightforward to relate any of the Langmuir numbers to TKE budgets in complex seas with misaligned wind and waves. The Stokes drift and Stokes

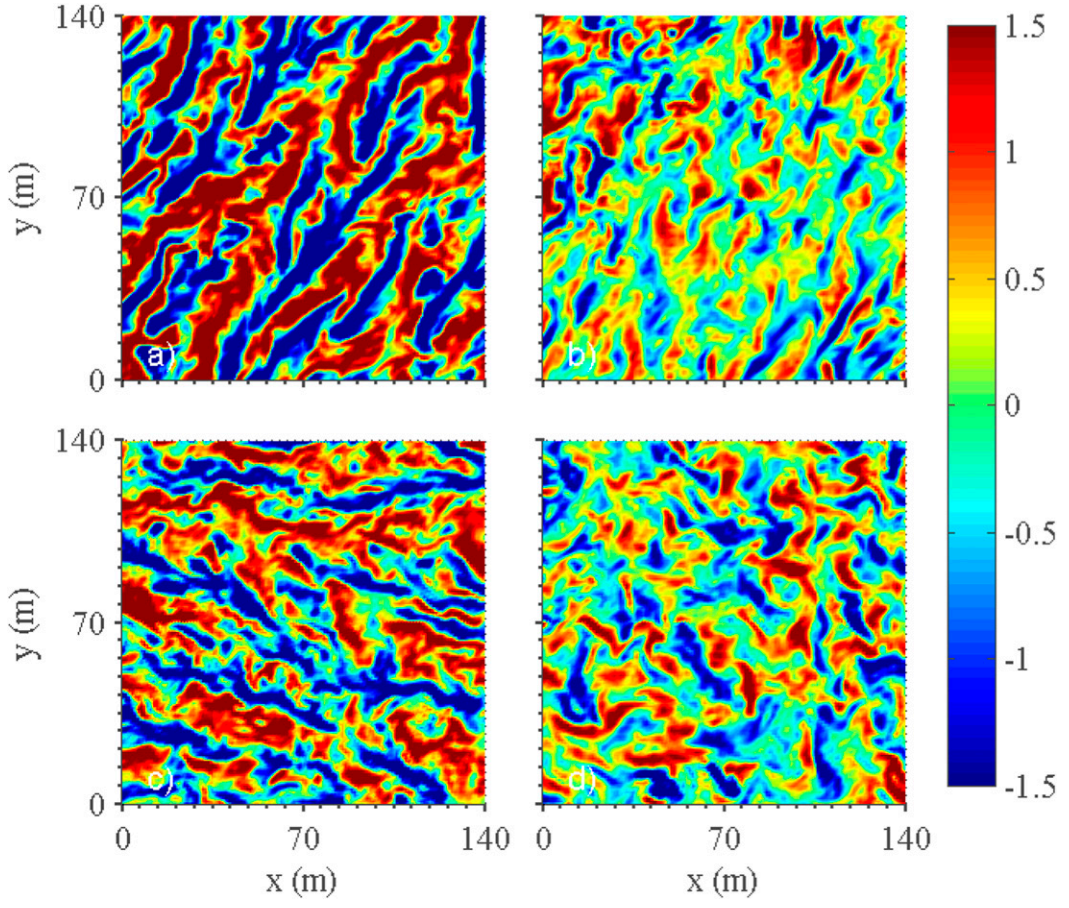

FIG. 14. Cross sections of vertical velocity normalized by u_* at days (top) 245.115 and (bottom) 245.285 for the (a),(c) LT and (b),(d) ST simulations. Cross sections are taken at the depth of maximum anisotropy coefficient R_t above $z/h = -0.5$.

drift direction have been averaged over 20% of the mixed layer as outlined by Harcourt and D'Asaro (2008). The Lagrangian shear direction is calculated via

$$\tan(\alpha_L) = \frac{\langle \partial v_L/\partial z\rangle_{0.2h}}{\langle \partial u_L/\partial z\rangle_{0.2h}}, \tag{13}$$

where u_L and v_L are the Lagrangian velocities in the x and y directions. Since the Lagrangian shear is a function of z, α_L is averaged over 0.2 of the mixed layer to allow for one angle in the Langmuir number formulation. The surface layer Langmuir number in Eq. (12) is plotted relative to the normalized bulk VVV. Directionality is also included in the normalized bulk VVV via

$$\frac{\langle w_T'^2\rangle_h}{[u_* \cos(\alpha_L - \Theta)]^2},$$

which projects the friction velocity u_* into the Lagrangian shear direction. The simple surface layer Langmuir number from Harcourt and D'Asaro (2008) is also examined,

$$\mathrm{La}_{\mathrm{SL}} = \sqrt{\frac{u_*}{|\langle \mathbf{u}_s\rangle_{0.2h}|}}, \tag{14}$$

and scaled relative to the normalized bulk VVV $\langle w_T'^2\rangle_h/u_*^2$ to investigate how important the misalignment is for the Langmuir number scaling.

Scaling the normalized bulk VVV with the modified Langmuir number, indicate that if directionality is included in the formulation, the results scale better (Fig. 15). During the time of maximum misalignment (days 245.2 to 245.4), the simple surface layer Langmuir number has many outliers (Figs. 15a,c). Most of those are removed when misalignment is taken into account (Figs. 15b,d). For the beginning and end of the simulations, when the wind and waves are relatively aligned, directionality is not as important. This suggests that the surface layer Langmuir number with directionality is an

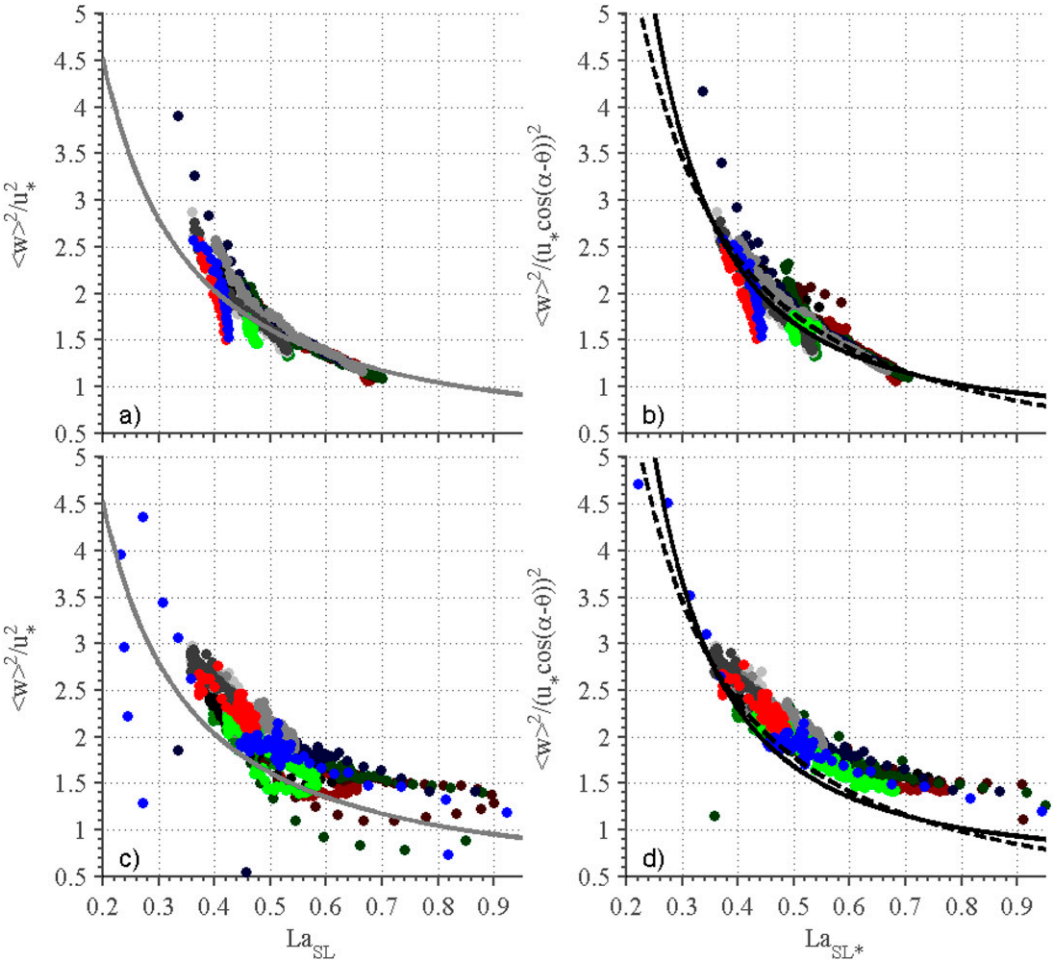

FIG. 15. (b),(d) Surface layer Langmuir number from Van Roekel et al. (2012) and the (a),(c) simple surface layer Langmuir number from Harcourt and D'Asaro (2008) scaled relative to the bulk VVV normalized by u_* or the projected u_*. All LT float simulation results (dots: Peak is red, Eye is blue, and Edge is green) and stationary simulation results are included (station 409 is black; all other colors represent the remaining stations shown in Fig. 1). (a) and (b) show the scaling results before the eye of Gustav has passed and (c) and (d) show the scaling results after the eye has passed over the locations. Also included are three proposed scalings from Van Roekel et al. (2012) (black, solid and dashed) and Harcourt and D'Asaro (2008) (gray) for the surface layer Langmuir number.

important parameter to parameterize LT during TCs. Some deviations from the scalings are expected because the simulations are fully transient where the previous scalings from Harcourt and D'Asaro (2008) and Van Roekel et al. (2012) have been developed with steady-state simulation results. Note that the data before and after the eye of Gustav passes have slight biases (Figs. 15b,d). Before the eye passes, the data (Fig. 15b) fall almost on top of the scalings from Van Roekel et al. (2012). After the eye passes, the results (Fig. 15d) fall above the scalings. One explanation for the differing scaling results before/after Gustav passes over the locations are history effects associated with transient forcing and differences in strongly forced and decaying turbulence. After the wind begins to reduce, the residual turbulence remains in the mixed layer longer than the changing forcing.

5. Discussion and conclusions

A large-eddy simulation was utilized to model the turbulence under Hurricane Gustav (2008) in an effort to better understand the importance of LT during tropical cyclones. A rational and straightforward approach has been used to simulate the upper-ocean response. NOAA's H*Wind was used to produce the time-dependent wind fields. WAVEWATCH III was used in concert with the wind fields to produce a time- and space-dependent wave field. Previous wind stress and drag coefficient parameterizations were used to drive the wave and LES models.

Comparison of LES results with Lagrangian float field observations indicate that LT plays an important role in upper-ocean mixing. Results strongly suggest that without LT effects simulated VVV underestimates the observed VVV. LT increases the VVV, indicating that it plays a significant role in upper-ocean turbulence dynamics. Consistent with observations, the LES predicts a suppression of VVV near the hurricane eye due to wind-wave misalignment. However, the observed suppression is stronger and of longer duration than the simulations indicate. Drag coefficient uncertainty, restratification under the eye, and breaking waves with bubble injection could play a role in reducing bulk VVV levels consistent with the observed suppression. LES results agree better with observations with a lower saturated drag coefficient, suggesting that the air–sea drag coefficient is relatively low in tropical cyclone conditions. Bulk VVV, a TKE budget analysis, and anisotropy coefficients of turbulent velocities all indicate that LT can suppress turbulence to levels closer to that of ST because of wave field variability.

Scaling the normalized bulk VVV versus the surface layer Langmuir number from Harcourt and D'Asaro (2008) and from Van Roekel et al. (2012) shows that misalignment between wind and waves is important for the strength of LT. The data indicate that the addition of directionality in the surface layer Langmuir number collapses the data closer to the scaling results from Van Roekel et al. (2012). A more complete turbulence scaling should take the effects of breaking waves into account (e.g., McWilliams et al. 2012). Furthermore, the Lagrangian shear eddy viscosity may be a nonmonotonic function of the turbulent Langmuir number because of its dependence on wave age (McWilliams et al. 2014).

Investigation of temperature profile evolution reveals that LT enhances mixed layer deepening, resulting in larger sea surface cooling compared with ST. The difference between the simulated sea surface cooling for LT versus ST is as much as a 0.3°C difference, and cooling occurs earlier and more rapidly with LT than ST, which will have implications for accurately predicting tropical cyclone strength (Emanuel et al. 2004). Note that for other tropical cyclone systems, ocean temperature changes could be larger than those observed here because salinity dominantly influenced density in our study.

This work suggests that LT critically influences upper-ocean response during tropical cyclones and must be considered for accurate TC predictions. The surface layer Langmuir number will provide guidance for the development of an upper-ocean boundary layer parameterization that explicitly depends on the sea state.

Acknowledgments. We acknowledge the support of the Office of Naval Research Grants N00014-08-1-0577 and N00014-10-1-0313, NSF Grant OCE0549887, and NSF Grant OCE1130678. We thank the U.S. Air Force Reserve Command 53rd Weather Reconnaissance Squadron Hurricane Hunters, the captain and crew of the R/V *Cape Hatteras*, and the engineers and technicians at APL/UW who made the observations possible. This research was also supported in part through the use of computational or staff resources provided by Information Technologies at the University of Delaware.

APPENDIX

Subgrid-Scale Model

The subgrid-scale fluxes are related to the resolved scale turbulent field through an eddy viscosity for momentum ν_M and the strain rate tensor S_{ij}:

$$\tau_{ij} = \nu_M \left(\frac{\partial \overline{u}_i}{\partial x_j} + \frac{\partial \overline{u}_j}{\partial x_i} \right). \tag{A1}$$

The eddy viscosity ν_M depends on the subgrid-scale turbulent kinetic energy and the mixing length. The eddy viscosity is

$$\nu_M = 0.1 l e^{1/2}, \tag{A2}$$

where e is the subgrid-scale contribution of the turbulent kinetic energy, and l is the mixing length. The mixing length, based on scaling arguments, is determined by the grid spacing of the LES model and the stability of the boundary layer. For neutral or unstable boundary layer conditions, the mixing length is defined by the grid resolution $l = \Delta s = (\Delta x \Delta y \Delta z)^{1/3}$. However, if the boundary layer is stable, the mixing length is defined as $l = 0.76 e^{1/2} [\alpha g (\partial T / \partial z)]^{-1/2}$. For stable stratification, the size of eddies can be smaller than the grid spacing and thus a more stringent mixing length has been defined (Deardorff 1980).

The eddy viscosity for scalars (e.g., temperature) is defined as

$$\nu_T = \left(1 + 2 \frac{l}{\Delta s} \right) \nu_M. \tag{A3}$$

This gives $\nu_T / \nu_M = 1$ as a lower limit when the stratification yields very stable boundary layer conditions. An upper limit of $\nu_T / \nu_M = 3$ is reached for a neutral or unstable boundary layer where scalar mixing is enhanced. The subgrid-scale density fluxes $\tau_{\rho j}$ are related to the resolved scales through the subgrid-scale temperature fluxes that are parameterized via

$$\tau_{Tj} = \nu_T \frac{\partial T}{\partial x_j}. \quad \text{(A4)}$$

The prognostic equation for the subgrid-scale turbulent kinetic energy, described by Deardorff (1973), is defined as follows:

$$\frac{\partial e}{\partial t} + \overline{u}_j \frac{\partial e}{\partial x_j} = \tau_{ij} \frac{\partial \overline{u}_i}{\partial x_j} + \alpha g \tau_{Tj} + \frac{\partial}{\partial x_j}\left(2\nu_M \frac{\partial e}{\partial x_j}\right) - \epsilon. \quad \text{(A5)}$$

The terms in Eq. (A5), from left to right, are the temporal rate of change of SGS TKE, advection of SGS TKE by the resolved velocity, production of SGS TKE by the resolved shear, SGS buoyancy production, SGS TKE diffusion, and dissipation. The assumption that was made to arrive at the flux divergence term was the downgradient diffusion assumption (Moeng 1984).

The dissipation ϵ is modeled by

$$\epsilon = \frac{Ce^{3/2}}{l}, \quad \text{(A6)}$$

where

$$C = 0.19 + 0.51 l (\Delta x \Delta y \Delta z)^{-1/3}. \quad \text{(A7)}$$

The subgrid-scale model, near the surface, is modified to better match with Monin–Obukhov similarity theory (Monin and Obukhov 1954; Sullivan et al. 1994; Moeng 1984; McWilliams et al. 1997).

REFERENCES

Belcher, S. E., and Coauthors, 2012: A global perspective on Langmuir turbulence in the ocean surface boundary layer. *Geophys. Res. Lett.,* **39,** L18605, doi:10.1029/2012GL052932.

Bender, M. A., and I. Ginis, 2000: Real-case simulations of hurricane–ocean interaction using a high-resolution coupled model: Effects on hurricane intensity. *Mon. Wea. Rev.,* **128,** 917–946, doi:10.1175/1520-0493(2000)128<0917:RCSOHO>2.0.CO;2.

Craik, A. D., and S. Leibovich, 1976: A rational model for Langmuir circulations. *J. Fluid Mech.,* **73,** 401–426, doi:10.1017/S0022112076001420.

D'Asaro, E. A., 2001: Turbulent vertical kinetic energy in the ocean mixed layer. *J. Phys. Oceanogr.,* **31,** 3530–3537, doi:10.1175/1520-0485(2002)031<3530:TVKEIT>2.0.CO;2.

——, 2003a: The ocean boundary layer below Hurricane Dennis. *J. Phys. Oceanogr.,* **33,** 561–579, doi:10.1175/1520-0485(2003)033<0561:TOBLBH>2.0.CO;2.

——, 2003b: Performance of autonomous Lagrangian floats. *J. Atmos. Oceanic Technol.,* **20,** 896–911, doi:10.1175/1520-0426(2003)020<0896:POALF>2.0.CO;2.

——, and C. McNeil, 2007: Air–sea gas exchange at extreme wind speeds measured by autonomous oceanographic floats. *J. Mar. Syst.,* **66,** 92–109, doi:10.1016/j.jmarsys.2006.06.007.

——, D. M. Farmer, J. T. Osse, and G. T. Dairiki, 1996: A Lagrangian float. *J. Atmos. Oceanic Technol.,* **13,** 1230–1246, doi:10.1175/1520-0426(1996)013<1230:ALF>2.0.CO;2.

——, J. Thomson, A. Shcherbina, R. Harcourt, M. Cronin, M. Hemer, and B. Fox-Kemper, 2014: Quantifying upper ocean turbulence driven by surface waves. *Geophys. Res. Lett.,* **41,** 102–107, doi:10.1002/2013GL058193.

Deardorff, J. W., 1973: The use of subgrid transport equations in a three-dimensional model of atmospheric turbulence. *J. Fluids Eng.,* **95,** 429–438, doi:10.1115/1.3447047.

——, 1980: Stratocumulus-capped mixed layers derived from a three-dimensional model. *Bound.-Layer Meteor.,* **18,** 495–527, doi:10.1007/BF00119502.

DeMaria, M., C. R. Sampson, J. A. Knaff, and K. D. Musgrave, 2013: Is tropical cyclone intensity guidance improving? *Bull. Amer. Meteor. Soc.,* **95,** 387–398, doi:10.1175/BAMS-D-12-00240.1.

Donelan, M., B. Haus, N. Reul, W. Plant, M. Stiassnie, H. Graber, O. Brown, and E. Saltzman, 2004: On the limiting aerodynamic roughness of the ocean in very strong winds. *Geophys. Res. Lett.,* **31,** L18306, doi:10.1029/2004GL019460.

Emanuel, K., C. DesAutels, C. Holloway, and R. Korty, 2004: Environmental control of tropical cyclone intensity. *J. Atmos. Sci.,* **61,** 843–858, doi:10.1175/1520-0469(2004)061<0843:ECOTCI>2.0.CO;2.

Fan, Y., I. Ginis, T. Hara, C. W. Wright, and E. J. Walsh, 2009: Numerical simulations and observations of surface wave fields under an extreme tropical cyclone. *J. Phys. Oceanogr.,* **39,** 2097–2116, doi:10.1175/2009JPO4224.1.

French, J. R., W. M. Drennan, J. A. Zhang, and P. G. Black, 2007: Turbulent fluxes in the hurricane boundary layer. Part I: Momentum flux. *J. Atmos. Sci.,* **64,** 1089–1102, doi:10.1175/JAS3887.1.

Gemmrich, J., 2012: Bubble-induced turbulence suppression in Langmuir circulation. *Geophys. Res. Lett.,* **39,** L10604, doi:10.1029/2012GL051691.

Grant, A. L. M., and S. E. Belcher, 2009: Characteristics of Langmuir turbulence in the ocean mixed layer. *J. Phys. Oceanogr.,* **39,** 1871–1887, doi:10.1175/2009JPO4119.1.

——, and ——, 2011: Wind-driven mixing below the oceanic mixed layer. *J. Phys. Oceanogr.,* **41,** 1556–1575, doi:10.1175/JPO-D-10-05020.1.

Harcourt, R. R., and E. A. D'Asaro, 2008: Large-eddy simulation of Langmuir turbulence in pure wind seas. *J. Phys. Oceanogr.,* **38,** 1542–1562, doi:10.1175/2007JPO3842.1.

——, and ——, 2010: Measurement of vertical kinetic energy and vertical velocity skewness in oceanic boundary layers by imperfectly Lagrangian floats. *J. Atmos. Oceanic Technol.,* **27,** 1918–1935, doi:10.1175/2010JTECHO731.1.

Holthuijsen, L. H., M. D. Powell, and J. D. Pietrzak, 2012: Wind and waves in extreme hurricanes. *J. Geophys. Res.,* **117,** C09003, doi:10.1029/2012JC007983.

Kenyon, K. E., 1969: Stokes drift for random gravity waves. *J. Geophys. Res.,* **74,** 6991–6994, doi:10.1029/JC074i028p06991.

Kukulka, T., A. J. Plueddemann, J. H. Trowbridge, and P. P. Sullivan, 2009: Significance of Langmuir circulation in upper ocean mixing: Comparison of observations and simulations. *Geophys. Res. Lett.,* **36,** L10603, doi:10.1029/2009GL037620.

——, ——, ——, and ——, 2010: Rapid mixed layer deepening by the combination of Langmuir and shear instabilities: A case study. *J. Phys. Oceanogr.,* **40,** 2381–2400, doi:10.1175/2010JPO4403.1.

——, ——, and P. P. Sullivan, 2013: Inhibited upper ocean restratification in nonequilibrium swell conditions. *Geophys. Res. Lett.,* **40,** 3672–3676, doi:10.1002/grl.50708.

Langmuir, I., 1938: Surface motion of water induced by wind. *Science,* **87,** 119–123, doi:10.1126/science.87.2250.119.

Large, W. G., and S. Pond, 1981: Open ocean momentum flux measurements in moderate to strong winds. *J. Phys. Oceanogr.,* **11,** 324–336, doi:10.1175/1520-0485(1981)011<0324:OOMFMI>2.0.CO;2.

——, J. C. McWilliams, and S. C. Doney, 1994: Oceanic vertical mixing: A review and a model with a nonlocal boundary layer parameterization. *Rev. Geophys.,* **32,** 363–403, doi:10.1029/94RG01872.

Li, M., C. Garrett, and E. Skyllingstad, 2005: A regime diagram for classifying turbulent large eddies in the upper ocean. *Deep-Sea Res. I,* **52,** 259–278, doi:10.1016/j.dsr.2004.09.004.

McWilliams, J. C., P. P. Sullivan, and C.-H. Moeng, 1997: Langmuir turbulence in the ocean. *J. Fluid Mech.,* **334,** 1–30, doi:10.1017/S0022112096004375.

——, J. R. Restrepo, and E. M. Lane, 2004: An asymptotic theory for the interaction of waves and currents in shallow coastal water. *J. Fluid Mech.,* **511,** 135–178, doi:10.1017/S0022112004009358.

——, E. Huckle, J.-H. Liang, and P. P. Sullivan, 2012: The wavy Ekman layer: Langmuir circulations, breaking waves, and Reynolds stress. *J. Phys. Oceanogr.,* **42,** 1793–1816, doi:10.1175/JPO-D-12-07.1.

——, ——, ——, and ——, 2014: Langmuir turbulence in swell. *J. Phys. Oceanogr.,* **44,** 870–890, doi:10.1175/JPO-D-13-0122.1.

Melville, W., 1996: The role of surface-wave breaking in air-sea interaction. *Annu. Rev. Fluid Mech.,* **28,** 279–321, doi:10.1146/annurev.fl.28.010196.001431.

Moeng, C.-H., 1984: A large-eddy-simulation model for the study of planetary boundary-layer turbulence. *J. Atmos. Sci.,* **41,** 2052–2062, doi:10.1175/1520-0469(1984)041<2052:ALESMF>2.0.CO;2.

Monin, A., and A. Obukhov, 1954: Basic laws of turbulent mixing in the surface layer of the atmosphere. *Contrib. Geophys. Inst. Acad. Sci. USSR,* **151,** 163–187.

Noh, Y., H. S. Min, and S. Raasch, 2004: Large eddy simulation of the ocean mixed layer: The effects of wave breaking and Langmuir circulation. *J. Phys. Oceanogr.,* **34,** 720–735, doi:10.1175/1520-0485(2004)034<0720:LESOTO>2.0.CO;2.

Plueddemann, A. J., J. A. Smith, D. M. Farmer, R. A. Weller, W. R. Crawford, R. Pinkel, S. Vagle, and A. Gnanadesikan, 1996: Structure and variability of Langmuir circulation during the surface waves processes program. *J. Geophys. Res.,* **101,** 3525–3543, doi:10.1029/95JC03282.

Polton, J. A., and S. E. Belcher, 2007: Langmuir turbulence and deeply penetrating jets in an unstratified mixed layer. *J. Geophys. Res.,* **112,** C09020, doi:10.1029/2007JC004205.

Pope, S. B., 2000: *Turbulent Flows.* Cambridge University Press, 802 pp.

Powell, M. D., S. H. Houston, L. R. Amat, and N. Morisseau-Leroy, 1998: The HRD real-time hurricane wind analysis system. *J. Wind Eng. Ind. Aerodyn.,* **77–78,** 53–64, doi:10.1016/S0167-6105(98)00131-7.

——, P. J. Vickery, and T. A. Reinhold, 2003: Reduced drag coefficient for high wind speeds in tropical cyclones. *Nature,* **422,** 279–283, doi:10.1038/nature01481.

——, and Coauthors, 2010: Reconstruction of Hurricane Katrina's wind fields for storm surge and wave hindcasting. *Ocean Eng.,* **37,** 26–36, doi:10.1016/j.oceaneng.2009.08.014.

Price, J. F., 1981: Upper ocean response to a hurricane. *J. Phys. Oceanogr.,* **11,** 153–175, doi:10.1175/1520-0485(1981)011<0153:UORTAH>2.0.CO;2.

——, R. A. Weller, and R. Pinkel, 1986: Diurnal cycling: Observations and models of the upper ocean response to diurnal heating, cooling, and wind mixing. *J. Geophys. Res.,* **91,** 8411–8427, doi:10.1029/JC091iC07p08411.

Sanford, T. B., P. G. Black, J. R. Haustein, J. W. Feeney, G. Z. Forristall, and J. F. Price, 1987: Ocean response to a hurricane. Part I: Observations. *J. Phys. Oceanogr.,* **17,** 2065–2083, doi:10.1175/1520-0485(1987)017<2065:ORTAHP>2.0.CO;2.

——, J. F. Price, and J. B. Girton, 2011: Upper-ocean response to Hurricane Frances (2004) observed by profiling EM-APEX floats. *J. Phys. Oceanogr.,* **41,** 1041–1056, doi:10.1175/2010JPO4313.1.

Shay, L. K., P. G. Black, A. J. Mariano, J. D. Hawkins, and R. L. Elsberry, 1992: Upper ocean response to Hurricane Gilbert. *J. Geophys. Res.,* **97,** 20 227–20 248, doi:10.1029/92JC01586.

Skyllingstad, E. D., and D. W. Denbo, 1995: An ocean large-eddy simulation of Langmuir circulations and convection in the surface mixed layer. *J. Geophys. Res.,* **100,** 8501–8522, doi:10.1029/94JC03202.

——, W. Smyth, and G. Crawford, 2000: Resonant wind-driven mixing in the ocean boundary layer. *J. Phys. Oceanogr.,* **30,** 1866–1890, doi:10.1175/1520-0485(2000)030<1866:RWDMIT>2.0.CO;2.

Smith, J. A., 1998: Evolution of Langmuir circulation during a storm. *J. Geophys. Res.,* **103,** 12 649–12 668, doi:10.1029/97JC03611.

Sullivan, P. P., J. C. McWilliams, and C.-H. Moeng, 1994: A subgrid-scale model for large-eddy simulation of planetary boundary-layer flows. *Bound.-Layer Meteor.,* **71,** 247–276, doi:10.1007/BF00713741.

——, ——, and W. K. Melville, 2007: Surface gravity wave effects in the oceanic boundary layer: Large-eddy simulation with vortex force and stochastic breakers. *J. Fluid Mech.,* **593,** 405–452, doi:10.1017/S002211200700897X.

——, L. Romero, J. C. McWilliams, and W. K. Melville, 2012: Transient evolution of Langmuir turbulence in ocean boundary layers driven by hurricane winds and waves. *J. Phys. Oceanogr.,* **42,** 1959–1980, doi:10.1175/JPO-D-12-025.1.

Terray, E., M. Donelan, Y. Agrawal, W. Drennan, K. Kahma, A. Williams, P. Hwang, and S. Kitaigorodskii, 1996: Estimates of kinetic energy dissipation under breaking waves. *J. Phys. Oceanogr.,* **26,** 792–807, doi:10.1175/1520-0485(1996)026<0792:EOKEDU>2.0.CO;2.

Tolman, H. L., 2009: User manual and system documentation of WAVEWATCH-III, version 3.14. NOAA/NWS/NCEP/MMAB Tech. Note 276, 220 pp. [Available online at http://polar.ncep.noaa.gov/mmab/papers/tn276/MMAB_276.pdf.]

Van Roekel, L., B. Fox-Kemper, P. Sullivan, P. Hamlington, and S. Haney, 2012: The form and orientation of Langmuir cells for misaligned winds and waves. *J. Geophys. Res.,* **117,** C05001, doi:10.1029/2011JC007516.

Zedler, S., T. Dickey, S. Doney, J. Price, X. Yu, and G. Mellor, 2002: Analyses and simulations of the upper ocean's response to Hurricane Felix at the Bermuda Testbed Mooring site: 13–23 August 1995. *J. Geophys. Res.,* **107,** 3232, doi:10.1029/2001JC000969.